Electronic Structure of Ru_2^{6+} Complexes with Electron-Rich Anilinopyridinate Ligands

Michael D. Roy,[1] Michael J. Trenerry,[1] Biswash Thakuri,[2] Samantha N. MacMillan,[3] Matthew D. Liptak,[2] Kyle M. Lancaster,[3] and John F. Berry[1,*]

[1] Department of Chemistry, University of Wisconsin-Madison, 1101 University Ave., Madison, Wisconsin 53706, United States
[2] Department of Chemistry, University of Vermont, Burlington, Vermont 05405, United States
[3] Department of Chemistry & Chemical Biology, Baker Laboratory, Cornell University, Ithaca, New York 14853, United States

Abstract

Diruthenium paddlewheel complexes supported by electron rich anilinopyridinate (Xap) ligands were synthesized in order to allow for the first in-depth structural and spectroscopic interrogation of monocationic $[Ru_2(Xap)_4Cl]^+$ species in the Ru_2^{6+} oxidation state. Despite paramagnetism of the compounds, ^{1}H NMR spectroscopy proved highly informative for determining the isomerism of the Ru_2^{5+} and Ru_2^{6+} compounds. While most compounds are found to have the polar (4,0) geometry, with all four Xap ligands in the same orientation, some synthetic procedures resulted in a mixture of (4,0) and (3,1) isomers, most notably in the case of the parent compound $Ru_2(ap)_4Cl$. The isomerism of this compound has been overlooked in previous reports. Electrochemical studies demonstrate that oxidation potentials can be tuned by the installation of electron donating groups to the ligands, increasing accessibility of the Ru_2^{6+} oxidation state. The resulting Ru_2^{6+} monocations were found to have the expected $(\pi^*)^2$ ground state, and an in-depth study of the electronic transitions by Vis/NIR absorption and MCD spectroscopy with the aid of TD-DFT allowed for the assignment of the electronic spectra. The empty δ^* orbital is the major acceptor orbital for the most prominent electronic transitions. Both Ru_2^{5+} and Ru_2^{6+} compounds were studied by Ru K-edge X-ray absorption spectroscopy; however, the rising edge energy insensitive to redox changes in the compounds studied due to the broad lineshape observed for 4d transition metal K-edges. DFT calculations indicate the presence of ligand orbitals at the frontier level, suggesting that further oxidation beyond Ru_2^{6+} will be ligand-centered rather than metal-centered.

Introduction

Diruthenium paddlewheel complexes with metal-metal multiple bonds are of interest for their applications in magnetism,[1-10] materials,[11-13] medicine,[14-20] molecular electronics,[21-27] and reactivity/catalysis.[28-33] The vast majority of these compounds contain the mixed-valent Ru_2^{5+} core supported by four monoanionic bridging ligands and one or two axial ligands. While these Ru_2^{5+} compounds are abundant and well-studied,[34, 35] we and others have recently explored the chemistry of diruthenium compounds in more oxidized states, to provide a foundation for applications in O- and N-atom transfer,[30-32, 36] sulfide oxidation,[37, 38] water oxidation,[39] and catalytic C-H amination reactions.[29]

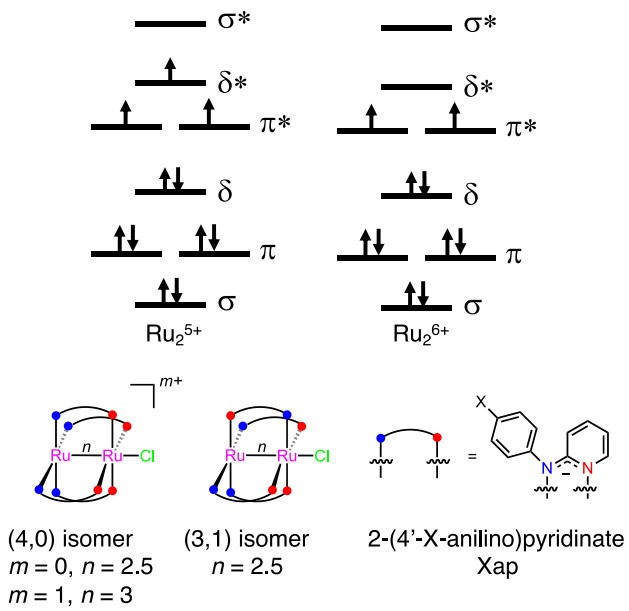

Figure 1.Top: Generic representation of Ru_2^{5+} (left) and Ru_2^{6+} (right) orbital energy level diagrams for complexes with equatorial N-atom donors. In contrast, carboxylate ligands typically have less donation from ligand π orbitals into the δ-symmetry metal orbitals, resulting in the metal δ orbitals being lower in energy than the π* orbitals. Bottom: Representation of $Ru_2(Xap)_4Cl$ compounds discussed in this work.*

Isolated Ru_2^{6+} compounds nearly uniformly bear strongly σ-donating organometallic axial ligands, resulting in a diamagnetic $S = 0$ ground electronic state.[8, 40-42] However, in the case of weak-field ligands relevant to catalysis, the paramagnetic $S = 1$ ground electronic state is expected (Figure 1). Representative examples include $Ru_2(hpp)_4Cl_2$ (hpp = 1,3,4,6,7,8-hexahydro-2*H*-pyrimido[1,2-*a*]pyrimidinate), the first $S = 1$ Ru_2^{6+} compound;[43, 44] Ren and coworkers' dimethylbenzamidinate (DMBA)-supported complex $Ru_2(DMBA)_4(NO_3)_2$ with labile nitrato axial ligands;[45] and $Ru_2(ap)_4Cl^+$, first reported by Cotton and Yokochi but without a definitive magnetic assignment due to the paramagnetic $FeCl_4^-$ counterion.[46] While catalytic intermediates invoke high-spin Ru_2^{6+} as well as Ru_2^{7+} and even Ru_2^{8+},[32, 36, 39] there are exceedingly few reports of crystallographically characterized high-spin Ru_2^{6+} compounds,[34] and the only crystallographically characterized Ru_2^{7+} compound, a terminal nitrido compound, was prepared and studied by X-ray photocrystallography starting from a Ru_2^{5+} azido compound.[28] To expand the field of high-spin, high-valent Ru_2 compounds, we set out to synthesize and study a systematic series of Ru_2^{6+} compounds supported by modifications of the well-known 2-anilinopyridinate (ap) ligand (Figure 1).

While the parent compound, $Ru_2(ap)_4Cl$, **1**, and its monocation $\mathbf{1}^+$ were first reported decades ago,[46, 47] only more recently has interest in this and related compounds as potential catalysts grown.[29, 33] Bear, Kadish, and coworkers explored the effect of electron withdrawing modifications of the ap ligand on the reduction potentials of $Ru_2(Xap)_4Cl$ compounds.[48-51] Our work emphasizes ap ligands having electron donating groups, which allows for facile structural characterization of ap-supported compounds in both the Ru_2^{5+} and Ru_2^{6+} oxidation states. The electronic structure of these Ru_2^{6+} compounds has been examined in detail with information obtained using SQUID magnetometry, electronic absorption and magnetic-circular dichroism (MCD) spectroscopies, and X-ray absorption spectroscopy. These data, along with computational models from density functional theory (DFT) were used to probe the nature of the Ru–Ru triple bond and the energies of the π* and δ* orbitals (Fig. 1). Ultimately, we contextualize our results in predictions from ligand field theory, including the nature of the features in the electronic spectra and the magnitude and sign of the zero field splitting. We further demonstrate that the oxidations beyond the Ru_2^{6+} level are likely to be ligand centered.

Results/Discussion

Synthesis, NMR Spectroscopy, and X-ray Crystallography

Derivatives of 2-anilinopyridine were prepared in 60-80% yield by solvent-free condensation of 2-bromopyridine or 2-bromo-5-methylpyridine with the corresponding 4-substituted aniline (Figure 3A).[52] Following the procedure established for the synthesis of **1**,[47] an excess of molten ligand was used to prepare, in good isomeric specificity, the (4,0) isomer of $Ru_2(Meap)_4Cl$ (**3**, >90% yield), $Ru_2(OMeap)_4Cl$ (**4**, >70% yield), and $Ru_2(a(Me)p)_4Cl$ (**5**, 64% yield), from diruthenium tetraacetate chloride ($Ru_2(OAc)_4Cl$) and 2-(4'-methylanilino)pyridine (H-Meap), 2-(4'-methoxylanilino)pyridine (H-OMeap), and 2-anilino-5-methylpyridine (H-a(Me)p), respectively (Figure 3B). Interestingly, when 2-(4'-chloroanilino)pyridine (H-Clap) and $Ru_2(OAc)_4Cl$ react under the same conditions, the result is an inseparable mixture of the (3,1) and (4,0) isomers of $Ru_2(Clap)_4Cl$ (**2'** and **2**, respectively), in low yield (26%, Figure 3C)). However, when H-Clap and $Ru_2(OAc)_4Cl$ react in refluxing toluene with an excess of LiCl present and a Soxhlet extractor charged with calcium carbonate,[53] the (4,0) isomer of $Ru_2(Clap)_4Cl$ (**2**) is exclusively obtained, though in low yield (35%, Figure 3D).

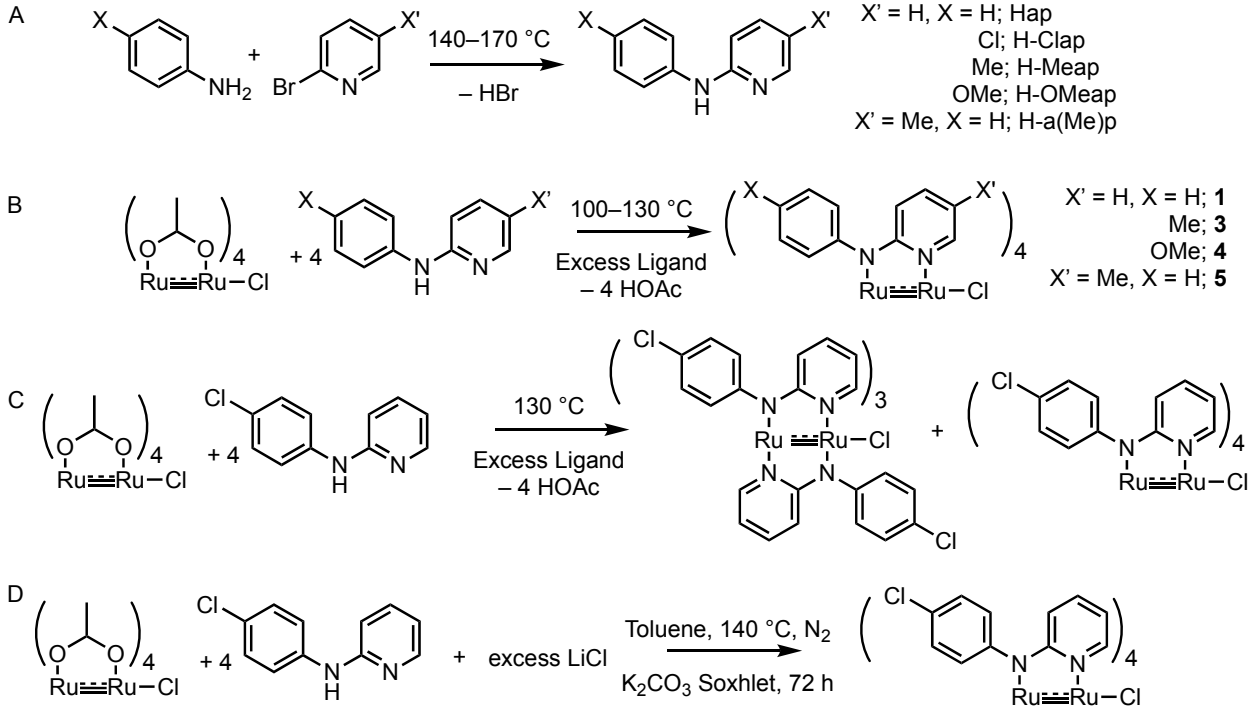

*Figure 3. A) Synthesis of anilinopyridine ligands; B) Reaction of $Ru_2(OAc)_4Cl$ with excess molten ligand; C) Synthesis of **2'** D) Preparation of **2**.*

The commercially available oxidant magic blue, tris(4-bromophenyl)ammoniumyl hexachloroantimonate, was found to oxidize readily all five Ru_2^{5+} compounds (**1**-**5**), and the Ru_2^{6+} products [**1**-**5**][$SbCl_6$] were isolated by precipitation from the CH_2Cl_2 reaction mixture upon addition of diethyl ether, separating the product from the soluble tris(4-bromophenyl)amine. Analogous reactions with tris(4-bromophenyl)ammoniumyl hexafluorophosphate[54] proceed in an identical manner to give the analogous salts with alternate counterions.

Despite the paramagnetism of the compounds, ^1H NMR spectroscopy was found to be extremely helpful in assessing both geometry and purity in both the Ru_2^{5+} and Ru_2^{6+} states.

Notably, the NMR spectrum of the known compound **1** has never been published previously. All the Ru_2^{5+} compounds have three strongly paramagnetically shifted singlet resonances at 35 – 37, -32 – -34, and -77 – -81 ppm, which have been assigned to the 3-5 positions on the pyridine, with the 6 position proton not being observed (Figure 4). Assignments were made through a combination of ^{1}H COSY and the preparation of **5**, which has a methyl-substituted pyridine ring (Figure S1, S2). In the NMR spectrum of **1**, a fourth resonance with equal integration value is detected at -1 ppm and assigned to the 4-position of the aryl ring, while the CH_3 group in **3** is observed at -6.74 ppm. Other aryl H atoms are not observed. Compound **4** is not sufficiently soluble for NMR analysis.

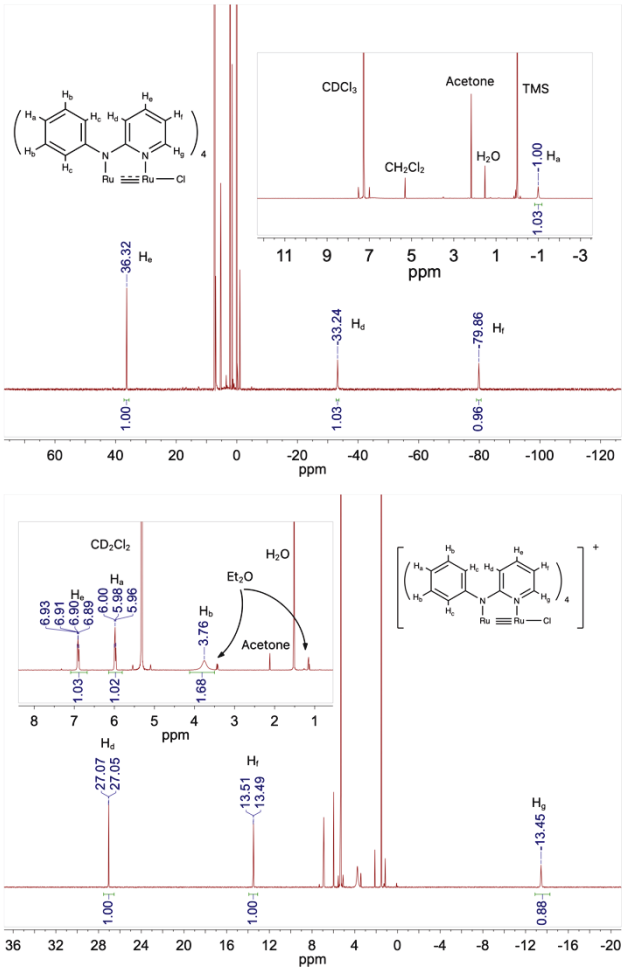

*Figure 4. ^{1}H NMR spectra of **1** (top) and [**1**][$SbCl_6$] (bottom).*

Upon oxidation, there are still three strongly paramagnetically shifted proton resonances observable, assigned to pyridine H atoms. These peaks at 24 – 27, 10 – 14, and -12 – -14 ppm are assigned as the H atoms at the 3, 5, and 6 positions, respectively, with the H atom in the 5 position appearing in the diamagnetic region of the spectrum between 6 and 7 ppm. More resonances are also observed for the aryl ring compared to the Ru_2^{5+} compounds, with the *para* H atom appearing at 5.98 ppm in $\mathbf{1}^+$ and the *meta* H atoms becoming detectable as a broad peak between 2 and 4 ppm. Only the *ortho* H atoms are not observed for Ru_2^{6+} compounds. Assignments were again made through a combination of ^{1}H COSY and comparison with [**5**][$SbCl_6$] (Figure S3, S4).

The geometry of the (3,1) isomer results in two equivalent and two electronically distinct ligands, causing the singlets each to split into a 2:1:1 pattern, which is observed for **2'**. Interestingly, preparations of **1** were found to contain a similar pattern of resonances (Figure S5), with crude material containing as much as 20% of the (3,1) isomer, which has previously not been recognized.[34, 55] Investigation into the crude material obtained using the published preparation of **1** revealed that both (3,1) and (4,0) isomers are obtained, but that the (3,1) isomer is significantly more soluble than the (4,0) isomer in methanol. Analytically pure (4,0)-**1** can therefore be obtained by sufficient washing. Beyond validating the usefulness of ^{1}H NMR spectroscopy for these compounds, this finding also indicates that (3,1)-**1** is an isolable product, and deliberate synthesis is likely possible.

Single crystals suitable for X-ray diffraction of **2**, **2'**, and **3** were grown by slow evaporation of dichloromethane solutions, while crystals of **4** were obtained from slow evaporation of a trifluoroethanol solution. As with the parent compound,[47] **2** and **3** also crystallize in the *C*2/*c* space group with the Ru–Ru axis oriented along the two-fold

crystallographic rotation axis. Compound **2'** also crystallizes in the *C*2/*c* space group, but the molecule does not reside on a special position. Compound **4** crystallizes in the tetragonal space group *P*4*nc*, with the molecule residing on the crystallographic four-fold rotation axis. For **1-4**, the molecules pack along the major rotation axis; however, in **4**, the packing is much closer, with the Ru–Cl distance elongated by ~0.1 Å and a much shorter intermolecular Cl···Ru distance to the terminal Ru of the adjacent molecule (~3 Å for **4** and ~5 Å for **1-3**) (Fig 5). This intermolecular interaction likely explains the significantly decreased solubility of **4** compared to **1-3**.

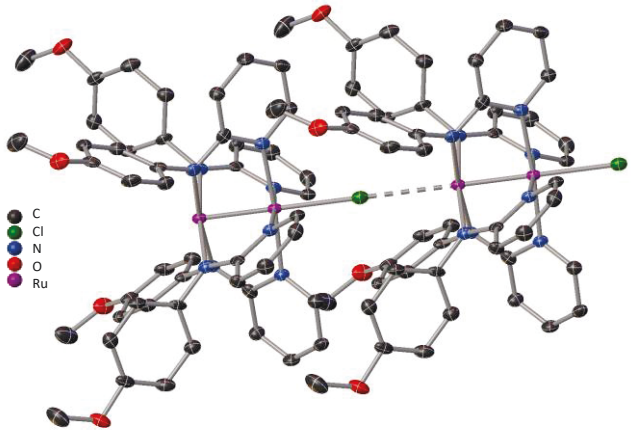

*Figure 5.Two molecules (eight asymmetric units) of **4** highlighting the intermolecular Cl···Ru interaction. H-atoms and individual atom labels omitted for clarity. Thermal ellipsoids drawn at 50% probability.*

Single crystals of [**1-4**][$SbCl_6$] were grown by vapor diffusion of diethyl ether into a saturated dichloromethane solution. Compounds [**1-3**][$SbCl_6$] crystallize in the monoclinic space group *P*2/*c* with both the complex and counterion positioned on adjacent crystallographic two-fold axes. Compound [**4**][$SbCl_6$] crystallizes in the tetragonal space group *I*4 with the complex and counterion alternating along the same crystallographic four-fold axis.

The key bond lengths across **2-4** are all similar to the parent **1**, aside from the Ru–Cl distances in **4** discussed above. In [**1-4**][$SbCl_6$], consistent bonding metrics are again observed. As expected for the increase in charge, the metal-ligand bond lengths decrease by ~ 0.02-0.03 Å. While the increase in Ru–Ru bond length (~0.03 Å) may be surprising, given that the formal bond order increases from 2.5 to 3 upon oxidation, this behavior is seen in other Ru_2 compounds and is attributed to the increased electrostatic repulsion between the two cationic Ru atoms, counterbalancing the small Ru–Ru contraction that would result from removing an electron from a δ* orbital.[34, 46]

Table 1. Key bonding metrics for all compounds.

Compound:	Ru–Ru (Å)	Ru–N_{py} (Å)	Ru–N_{an} (Å)	Ru–Cl (Å)	Reference
1	2.275(3)[a]	2.10[2]	2.03[2]	2.437(7)	[47]
2'	2.284(1)	2.100(3), 2.108(3), 2.089(3), 2.040(3)[b]	2.053(3), 2.020(3), 2.026(3), 2.086(3)[b]	2.474(2)	This work
2	2.276(1)	2.104[6]	2.033[6]	2.471(2)	This work

3	2.2781(9)	2.100[3]	2.030[3]	2.465(1)	This work
4	2.284(1)	2.078(5)	2.069(5)	2.586(6)	This work
[**1**][$FeCl_4$]	2.301(1)	2.09[1]	2.01[1]	2.419(2)	[46]
[**1**][$SbCl_6$]	2.3022(6)	2.081[2]	2.005[2]	2.4248(7)	This work
[**2**][$SbCl_6$]	2.2964(7)	2.089[2]	2.002[2]	2.4430(8)	This work
[**3**][$SbCl_6$]	2.302(1)	2.084[4]	1.999[4]	2.444(2)	This work
[**4**][$SbCl_6$]	2.296(1)	2.077(4)	2.009(3)	2.452(3)	This work

[a] Digits in curved brackets are ESDs for a single measured value, while digits in square brackets are ESDs which have been propagated for multiple averaged measured values.
[b] In **2'**, the Ru–N distance depends on which Ru atom is involved rather than the nature of the N atom, as indicated by the Ru–N distances of the ligand with the minority orientation.

Table 2. Crystallographic experimental data for all compounds.

Compound	**2'**	**2**	**3**	**4**	**[1][SbCl$_6$]**	**[2][SbCl$_6$]**	**[3][SbCl$_6$]**	**[4][SbCl$_6$]**
Formula	$C_{44}H_{32}Cl_5N_8Ru_2$	$C_{44}H_{32}Cl_5N_8Ru_2$	$C_{48}H_{44}ClN_8Ru_2$	$C_{48}H_{44}ClN_8O_4Ru_2$	$C_{44}H_{36}Cl7N_8Ru_2Sb$ • 0.95 CH_2Cl_2	$C_{44}H_{32}Cl_{11}N_8Ru_2Sb$ • 0.97 CH_2Cl_2	$C_{48}H_{44}Cl_7N_8Ru_2Sb$	$C_{48}H_{44}Cl_7N_8O_4Ru_2Sb$
Formula weight	1052.16	1052.16	970.50	1034.50	1329.53	1469.17	1304.95	1368.95
Temperature/K	100.01	100.01	100	100.01	100.0	100.0	99.99	100.01
Crystal system	Monoclinic	Monoclinic	Monoclinic	Tetragonal	Monoclinic	Monoclinic	Monoclinic	Tetragonal
Space group	*C*2/c	*C*2/c	*C*2/c	*P*4nc	*P*2/c	*P*2/c	*P*2/c	*I*4
a/Å	24.098(9)	24.016(8)	24.204(8)	16.000(1)	12.706(3)	12.722(3)	12.030(4)	10.330(3)
b/Å	9.742(4)	10.203(4)	10.080(3)	16.000(1)	9.559(2)	10.507(3)	10.327(5)	10.330(3)
c/Å	35.90(2)	20.428(8)	20.79(1)	7.8460(9)	20.288(6)	20.169(5)	21.603(8)	25.049(7)
α/°	90	90	90	90	90	90	90	90
β/°	96.42(2)	123.74(2)	124.33(1)	90	99.171(4)	98.19(1)	98.20(2)	90
γ/°	90	90	90	90	90	90	90	90
Volume/Å^3	8376(6)	4162(3)	4188(3)	2008.6(4)	2433(1)	2669(1)	2657(2)	2673(2)
Z	8	4	4	2	2	2	2	2
ρ_{calc}g/cm^3	1.669	1.679	1.539	1.710	1.815	1.828	1.631	1.701
μ/mm^{-1}	1.084	1.091	0.830	7.187	1.696	1.752	1.459	1.460
Radiation	MoKα (λ = 0.71073)	MoKα (λ = 0.71073)	MoKα (λ = 0.71073)	CuKα (λ = 1.54178)	MoKα (λ = 0.71073)	MoKα (λ = 0.71073)	MoKα (λ = 0.71073)	Mo Kα (λ = 0.71073)
R_{int}	0.1165	0.1237	0.0765	0.1029	0.0353	0.0367	0.1061	0.0704
Data/restraints/parameters	8591/0/532	3833/0/268	6146/0/270	1846/1/146	9270/0/308	10168/0/326	6592/0/303	4111/1/164
Goodness-of-fit on F^2	1.015	1.013	1.024	1.066	1.043	1.028	0.998	1.051
Final R indexes	R_1 = 0.0435	R_1 = 0.0408	R_1 = 0.0362	R_1 = 0.0325	R_1 = 0.0211	R_1 = 0.0198	R_1 = 0.0420	R_1 = 0.0297
[I>=2σ (I)][a, b]	wR_2 = 0.0751	wR_2 = 0.0750	wR_2 = 0.0750	wR_2 = 0.0733	wR_2 = 0.0484	wR_2 = 0.0450	wR_2 = 0.0657	wR_2 = 0.0649
Final R indexes	R_1 = 0.0806	R_1 = 0.0730	R_1 = 0.0582	R_1 = 0.0506	R_1 = 0.0258	R_1 = 0.0260	R_1 = 0.0908	R_1 = 0.0380
[all data]	wR_2 = 0.0853	wR_2 = 0.0843	wR_2 = 0.0819	wR_2 = 0.0803	wR_2 = 0.0499	wR_2 = 0.0471	wR_2 = 0.0778	wR_2 = 0.0675

[a] $R_1 = \sum||F_o| - |F_c||/\sum|F_o|$. [b] $wR_2 = [\sum[w(F_o^2 - F_c^2)^2]/\sum[w(F_o^2)^2]]^{1/2}$, $w = [(\sigma_{F_o^2})^2 + a^2[(1/3)F_o^2 + (2/3)F_c^2]^2]^{-1}$

Electrochemical Studies

The low solubilities of **2**-**4** prevented electrochemical analysis on the Ru_2^{5+} compounds directly. Therefore, the more soluble [**1**-**4**][PF_6] were used as analytes. Half-wave potentials ($E_{1/2}$ in V vs $Fc^{0/+}$ in CH_2Cl_2) of the $Ru_2^{4+/5+}$, $Ru^{5+/6+}$, and $Ru^{6+/7+}$ redox couples are plotted for complexes [**1**-**4**]PF_6 as functions of the sum of the Hammett parameters for the ligands' aryl functional groups (Figure 6; $\sum \sigma = 4\sigma_{Ar}$). For all three redox events, novel compounds [**2**-**4**][PF_6] match the linear free energy relationships previously observed for other (4,0) diruthenium complexes with methyl and fluoro-substituted anilinopyridinate ligands,[48, 56] demonstrating that these trends continue in the cathodic direction for complexes bearing more electron-donating substituents such as -OMe and -Me. As a point of comparison, the slope for the relationship $\Delta E_{1/2} = E_{1/2}(X) - E_{1/2}(H) = \rho(4\sigma)$, where ρ is the slope and σ is the Hammett parameter for the ligand substituent, is 0.116 V for the $Ru_2^{5+/6+}$ redox couple, while the well-studied diarylformamidinate (DArF) complexes exhibit a smaller slope of $\rho = 0.085$ V[57] for the $Ru_2^{5+/6+}$ redox couple of $Ru_2(DArF)_4Cl$[58] and $\rho = 0.087$ V for the $Mo_2^{4+/5+}$ redox couple of $Mo_2(DArF)_4$,[59, 60] though these compounds exhibit wider overall redox ranges due to the eight total substituents.

To assess the chemical reversibility of individual redox couples, we collected voltammograms of isolated redox features at multiple scan rates (Figures S6-S9). The $Ru_2^{4+/5+}$ redox couples showed generally poor chemical reversibility in all four complexes, presumably due to the loss of the axial -Cl ligand upon reduction to the Ru_2^{4+} oxidation state. By contrast, the $Ru_2^{5+/6+}$ and $Ru_2^{6+/7+}$ redox couples displayed quasireversible to fully reversible features. The $Ru_2^{6+/7+}$ features of compound [**2**][PF_6] uniquely showed two distinct redox events and we report both $E_{1/2}$ values, resolved by differential pulse voltammetry (Figure S10), in our Hammett analysis. Further discussion of oxidations beyond the Ru_2^{6+} oxidation state is provided in the *Computational Studies* section.

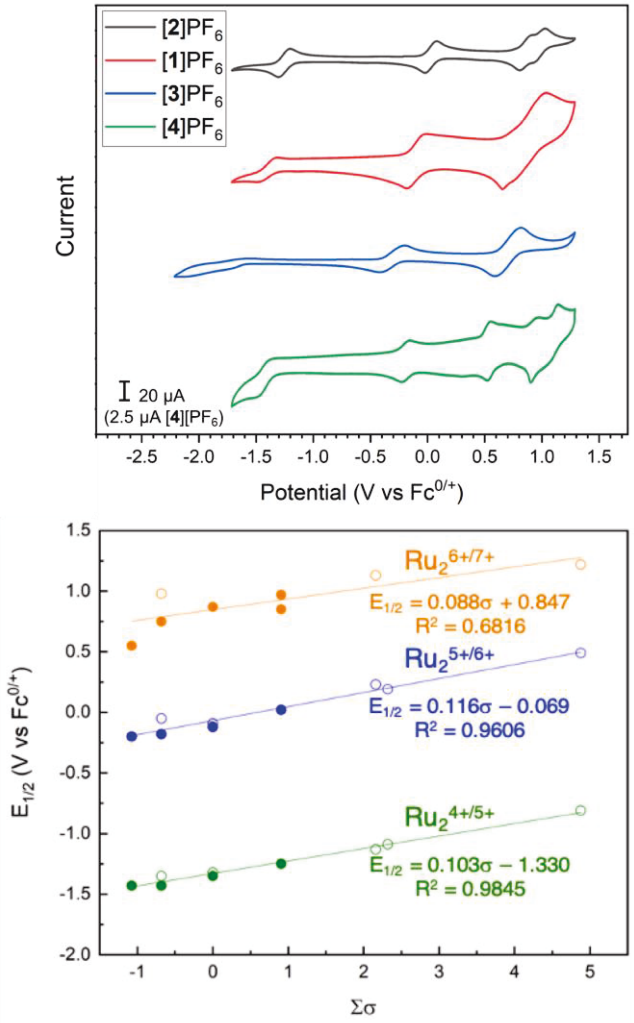

*Figure 6. Top: Representative cyclic voltammograms of [**1**-**4**][PF$_6$], collected for 1 mM [Ru$_2$] and 100 mM Bu$_4$NPF$_6$ solutions in CH$_2$Cl$_2$ at a 100 mV/s scan rate. Bottom: Linear free energy relationships for the redox reactions of (4,0) Ru$_2$(L)$_4$Cl complexes examined by this work (●= [**1**-**4**][SbCl$_6$]) and in previous work by Bear and Kadish[48] (o, L = 2-CH$_3$ap, ap, 2-Fap, 2,6-F$_2$ap, 2,5-F$_2$ap, 2,4,6-F$_3$ap, or F$_5$ap). Half-wave potentials are shown for the Ru$_2^{4+/5+}$ (green trace), Ru$^{5+/6+}$ (blue trace), and Ru$^{6+/7+}$ (orange trace) redox couples and are reported versus the Fc$^{0/+}$ redox couple in CH$_2$Cl$_2$. Half-wave potentials originally reported by Bear and Kadish versus SCE in CH$_2$Cl$_2$ have been converted to the Fc$^{0/+}$ reference according to Ref.61.*

X-ray Absorption Spectroscopy

Ru K-edge XAS data obtained for **1**, [**1**][PF$_6$] and [**1**][SbCl$_6$] are shown in Figure 7. None of the spectra exhibit resolved pre-edge (1s → 4d) features; these features are generally absent in conventionally-measured 4d transition metal K-edges due to core-hole lifetime broadening.[62-64] The position of the rising edge for all three compounds is invariant (22,111 eV), despite oxidation from Ru$_2^{5+}$ to Ru$_2^{6+}$. In a prior report of Ru$_2$ XAS, a 1eV shift was observed upon oxidation from Ru$_2^{5+}$ to Ru$_2^{7+}$ (Table 3).[65] Given this precedent, a 0.5 eV shift is predicted for the present redox pair, which is presumably unresolved due to the aforementioned line broadening.

The EXAFS region for **1** (Figure S11 and Table S1) was fitted using a model featuring 4 inner-sphere N scatterers with Ru−N = 2.075 Å, 1 Ru scatterer with Ru−Ru = 2.278 Å, 0.5 Cl

scatterer with Ru−Cl = 2.735 Å and 4 distal N scatterers with Ru−N = 3.004 Å. The Ru−Ru distance is in excellent agreement with the reported crystal structure (2.278(5) Å and 2.276(4) Å for EXAFS and X-ray, respectively). Fitting of the EXAFS region for the monocations (Figure S12-S13 and Tables S2-S3) was accomplished with the similar scattering paths. The elongation of the Ru−Ru distance upon oxidation observed in the crystal structure of [**1**][$SbCl_6$] is borne out in the EXAFS analysis, at 2.313(6) Å for [**1**][PF_6] and 2.307(8) Å for [**1**][$SbCl_6$], indicating that the effectively superimposable XANES correspond to unique compounds.

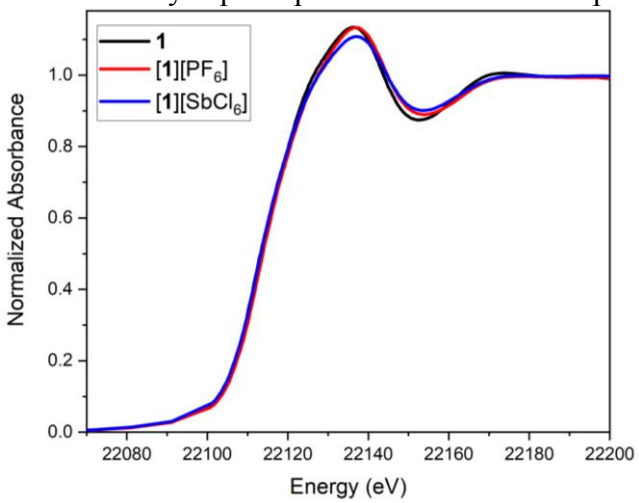

*Figure 7. Ru K-edge XANES data obtained for **1**, [**1**][PF_6] and [**1**][$SbCl_6$].*

Table 3. Rising K-edge energies for Ru_2 complexes (dPhf = N,N'-diphenylformamidinate).

Compound	Ru_2 Oxidation State	Rising Edge (eV)	Reference
1	Ru_2^{5+}	22,111	This work
[**1**][PF_6]	Ru_2^{6+}	22,111	This work
[**1**][$SbCl_6$]	Ru_2^{6+}	22,111	This work
$Ru_2(dPhf)_4N_3$	Ru_2^{5+}	22,116.5	[65]
$Ru_2(dPhf)_4N$	Ru_2^{7+}	22,117.9	[65]

Electronic Absorption and MCD Spectroscopies

Compounds **1**-**3** are green solids, while **4** is brown (Figure S14). However, when dissolved in CH_2Cl_2, all **1**-**4** are green with nearly identical visible light absorption spectra (Figure S15). In previous work, we were able to assign the lowest energy electronic transition as mainly having LMCT character, with partial $\delta \rightarrow \pi^*$ character.[35] Upon oxidation, [**1**-**4**][$SbCl_6$] are dark red solids, and [**1**-**3**][$SbCl_6$] are red in solution while [**4**][$SblCl_6$] is purple (Figure S16).

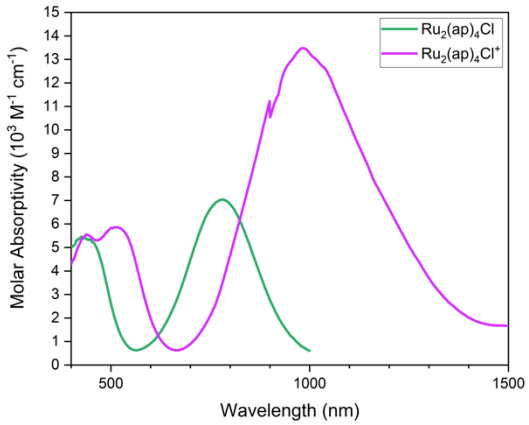

*Figure 8. Vis-NIR electronic spectra of **1** and [**1**][SbCl$_6$] in CH$_2$Cl$_2$. The discontinuity in the spectrum of [**1**][SbCl$_6$] at 900 nm is due to a change from a UV-Vis to a NIR detector.*

Spectroscopically, the two features in the Ru_2^{5+} spectrum shift to lower energy and the lower energy band increases in intensity, with the higher energy feature splitting into two (Figure 8). To better understand the electronic transitions contributing to the spectrum, MCD spectroscopy was employed. The MCD selection rules are such that d-d transitions are comparatively more intense than charge transfer transitions. The absorption and MCD spectra were iteratively fitted with Gaussian peaks, and those peaks correlated to transitions predicted *via* time-dependent density functional theory (see *Computational Studies* below). Figure 9 shows that the low-energy absorption band can be modeled as a single transition with negligible MCD intensity, and the low energy transitions primarily involve excitation to the δ* orbitals. The lower energy and greater intensity of these transitions compared to those in **1** are consistent with removal of the single δ* electron in **1**, and significantly more LMCT character in $\mathbf{1}^+$. Of the higher energy bands, the red-shifted band at ~550 nm also involves excitation to the now empty δ* orbital, while the band at ~450 nm, which is unshifted relative to **1**, involves excitation from and to orbitals orthogonal to the δ*.

Table 4. Transition assignments for experimental and calculated spectra.

Observed Band	**Observed Energy (cm^{-1})**	**Observed ε (M^{-1} cm^{-1})**	**Calculated Band**	**Calculated Energy (cm^{-1})**	**Calculated ε[a] (M^{-1} cm^{-1})**	**Assignment**
I	5836	1414	i[b]	5056	887	*e*(N) → δ*(Ru$_2$)
II	7403	0	ii[b]	10014	2020	*e*/*a*(N) → δ*/π* (Ru$_2$)
III	7800	0	iii[b]	10308	892	*a*(N) → π*(Ru$_2$)
IV	10175	13069	iv[b]	11907	14734	*e*(N)/π*(Ru$_2$) → δ*(Ru$_2$)
V	13049	760	v[b]	15622	555	Ligand aryl → δ*(Ru$_2$)
VI	16118	0	vi[b]	17513	1052	Ligand aryl → δ*(Ru$_2$)
VII	18679	2753	vii[b]	18228	8047	Ligand aryl/π_{nb}(Ru$_2$Cl) → δ*(Ru$_2$)
VIII	19082	2464	viii	18916	5052	Ligand aryl/δ(Ru$_2$) → δ*(Ru$_2$)
IX	21660	2820	ix$_a$[b] ix$_b$[b]	19521 19739	1155 2969	Ligand aryl → δ*(Ru$_2$) *e*(N) → σ*(Ru$_2$)

X	23439	3267	x_a[b]	22382	1289	$\sigma_{nb}(Ru_2Cl)$/Ligand →
			x_b[b]	22891	2991	$\pi^*(Ru_2)$
						$e(N)/\pi^*(Ru_2) \rightarrow \sigma^*(Ru_2)$
XI	26058	2135	xi	25220	1749	$\pi_{nb}(Ru_2Cl) \rightarrow \pi^*(Ru_2)$
XII	28007	3351	xii	31027	3367	Ligand pyr → $\pi^*(Ru_2)$

[a]ε calculated using Gaussian line width of 2000 cm^{-1}. [b]Two near-degenerate transitions are averaged to calculate energy and ε.

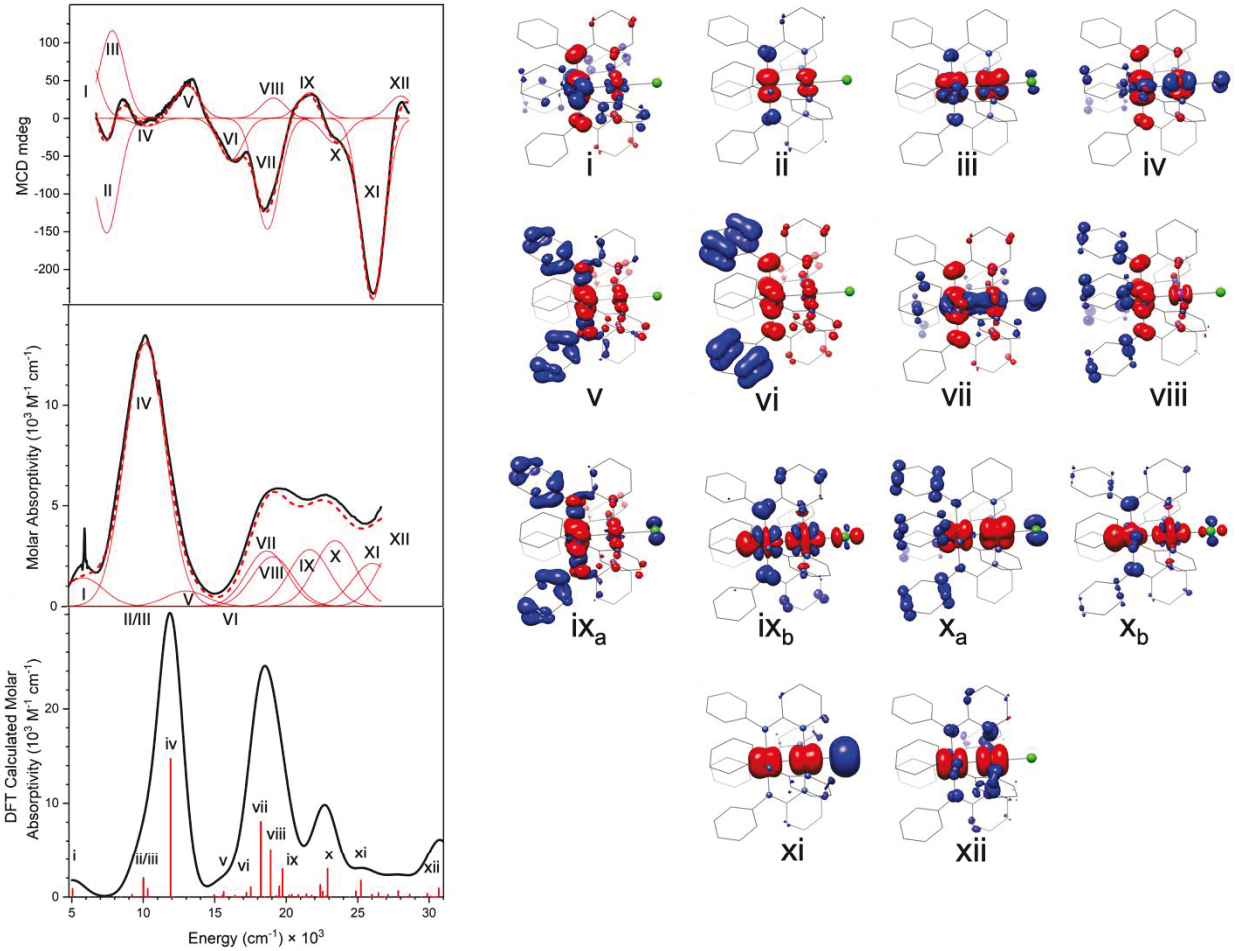

*Figure 9. MCD (top), Vis-NIR (middle), and TD-DFT transitions (bottom) of **1** and [**1**]$SbCl_6$ in CH_2Cl_2* with electron density difference maps plotted to the right, where blue and red indicate the loss and gain of electron density, respectively.

Magnetometry

The electronic structure of **1** has been studied previously, and the $S = 3/2$ ground electronic state is evident from EPR spectroscopy and SQUID magnetometry.[35] Based on the nearly identical spectroscopic features of **1**–**4**, we assign $S = 3/2$ as the ground electronic state for all of the Ru_2^{5+} compounds discussed herein.

In comparison, Ru_2^{6+} compounds can exhibit $S = 0$, 1, or 2 ground electronic states. The cation $[\mathbf{1}]^+$ was previously studied as a salt with the $FeCl_4^-$ counterion; due to the paramagnetism of the anion, magnetic susceptibility measurements of [**1**][$FeCl_4$] were not performed. Nevertheless, an $S = 1$ ground state was inferred from structural arguments.[46] While the paramagnetic shifting of the ^{1}H NMR spectra reported here are suggestive of an $S = 1$ ground state, variable temperature magnetic susceptibility of [**1**][$SbCl_6$] was measured to confirm this assignment (Figure 10). At room temperature, a $\chi \cdot T$ value of ~ 1.3 emu·K/mol is observed,

somewhat higher than the spin-only value expected for $S = 1$ (1.0 emu·K/mol), but nowhere near as high as expected for $S = 2$ (3.0 emu·K/mol). As temperature is lowered, the $\chi \cdot T$ data show a dramatic decrease, reaching ~ 0 emu·K/mol at the lowest temperature recorded. This behavior is consistent with an extraordinarily large zero-field splitting of the $S = 1$ state, as has been documented for other Ru_2^{6+} compounds.[66, 67] The data were modelled as an $S = 1$ system using a fixed isotropic g factor of 2.00 and large, positive axial zero-field splitting ($D = 196$ cm^{-1}). Free refinement of isotropic or anisotropic g factors did not meaningfully improve the quality of the model. Though few other $S = 1$ Ru_2^{6+} examples are known, reported values of D range from 168 to 261 cm^{-1}.[66, 67] A large temperature-independent paramagnetism term (1.34 10^{-3} emu/mol) was included to account for the larger-than-expected value for the room temperature magnetic susceptibility.

The trend in the χT plot toward zero at low temperatures indicates that the lowest energy m_s state is the $m_s = 0$ term of the $S = 1$ multiplet. This allows for unambiguous assignment of the sign of the zero field splitting as positive. Due to the large zero field splitting and $m_s = 0$ ground state, no saturation behavior is observed in low temperature magnetization measurements up to 7 T (Figure S17). As a result, the VT magnetic susceptibility data cannot be simultaneously fitted with reduced magnetization data, preventing the rhombic component of the zero field splitting, E, from being modeled, as the fit of the susceptibility data alone is insensitive to E.

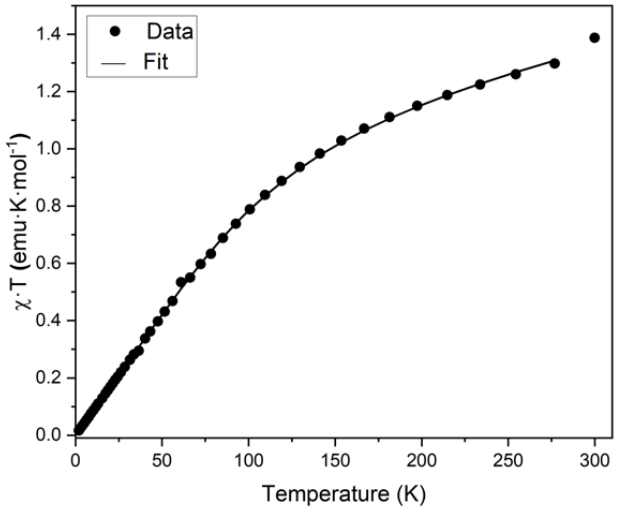

*Figure 10. Variable temperature SQUID magnetometry data for [**1**]SbCl$_6$.*

Table 5. Fitting parameters for magnetic data.

	g	D (cm^{-1})	E (cm^{-1})	zJ (cm^{-1})	TIP (emu/mol)	Residual	Reference
1	2.00 (fixed)	56.9(8)	15(1)	–0.188(4)	1.59(2) × 10^{-3}	1.8 × 10^{-3}	[35]
[**1**][SbCl$_6$]	2.00 (fixed)	195.8(8)	Not Fitted	Not Fitted	1.34(1) × 10^{-3}	1.4 × 10^{-3}	This work

*Residuals calculated as the sum of squares between experimental and calculated data points.[68]

Resonance Raman Spectroscopy

To probe the Ru–Ru bond stretching frequency as a function of Ru_2 oxidation state, resonance Raman spectroscopy was performed on a frozen CH_2Cl_2 solution of [**1**][PF_6] using 514 nm excitation (Figure 11). A stretch at 334 cm^{-1} in the spectrum matches well with the calculated Ru–Ru stretching frequency of 334 cm^{-1} (see below). In **1**, the Ru–Ru stretch is coupled with a rocking motion of the pyridine, giving a Fermi pair of vibrations at 345 and 421 cm^{-1}.[35] As indicated by the crystallographic data, the Ru-Ru bond length is longer for the Ru_2^{6+} compound than the Ru_2^{5+} compound, despite the increase in formal bond order. This change is consistent with the decrease in bond stretching frequency. These data can be compared to the $[Ru(OEP)]_2^{n+}$ (OEP = octaethylporphyrin, n = 0, 1, 2) series, where the Ru–Ru stretching frequency increases from 301 to 310 cm^{-1} upon oxidation from Ru_2^{5+} to Ru_2^{6+} (Table 6).[69] In this system, however, the bond length are estimated to decrease from 2.33 to 2.30 Å. Despite similar Ru–Ru bond lengths in the Ru_2^{6+} examples, the higher stretching frequency for [**1**][PF_6] clearly indicates that the anilinopyridinate-supported Ru–Ru bond is stronger. Furthermore, the electrostatic repulsion between the Ru cations contributes more to the observed Ru–Ru distance in the anilinopyridinate compounds than the removal of antibonding electrons, contrary to the OEP system studied earlier.

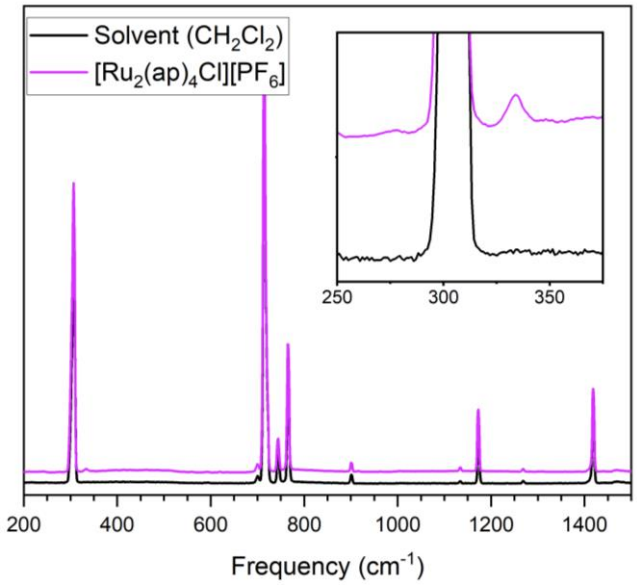

Figure 11. Resonance Raman spectra of [1][PF_6] in frozen CH_2Cl_2 (purple) and pure frozen CH_2Cl_2 (black).

Table 6. Ru–Ru bond distances and stretching frequencies for $Ru_2(ap)_4Cl^{0/+}$ and $[Ru(OEP)]_2^{+/2+}$.

Compound	Ru–Ru distance (Å)	Ru–Ru stretching frequency (cm^{-1})	Reference
1	2.275(3)	345 and 421 (Fermi)	[35, 47]
$\mathbf{1}^{+}$ [a]	2.3022(6)	334	This work
$[Ru(OEP)]_2^{+}$ [b]	2.33[c]	301	[69]
$[Ru(OEP)]_2^{2+}$ [b]	2.30[c]	310	[69]

[a] Crystallographic distance reported for [**1**][$SbCl_6$] while resonance Raman reported for [**1**][PF_6].
[b] All data reported with BF_4^- counterions.
[c] Bond distances estimated from empirical bond distance / force constant correlations.

Computational Studies

DFT calculations, including predictions of the physical properties discussed above, were performed to provide a detailed electronic structure consistent with experimental measurements. Optimized geometries for **1**-**4** and [**1**-**4**]$^+$ were calculated based on initial crystal structure coordinates. The calculated bond distances were in good agreement with experimental values, with Ru–Ru distances overestimated by only ~0.03 Å, and Ru–Cl and Ru–N distances overestimated by ~ 0.06 Å, with **4** having the Ru–Cl distance underestimated due to the aforementioned elongation caused by intermolecular interactions observed in the crystal structure. The calculated redox potentials for the $Ru_2^{5+/6+}$ couple correlate well with experimental values, though a constant offset is observed, consistent with other B3LYP calculations of redox potentials.[70] Importantly, the slope of the calculated redox potentials as a function of Hammett parameters, 0.13 V/σ, is in good agreement with the experimental slope, 0.12 V/σ (Figures 6, S18). As noted above, the calculated vibrational frequency of the Ru–Ru stretch and electronic transitions modeled *via* TD-DFT matched well with experiment, leading further credence to the validity of the computational model.

The electronic ground state of **1** is known to be $(\pi^*)^2(\delta^*)^1$, and the electronic ground state of the Ru_2^{6+} $S = 1$ compounds investigated here is expected to be $(\pi^*)^2$. DFT calculations support these ground states for [**1**-**4**] and [**1**-**4**]$^+$, though careful analysis reveals filled ligand-based orbitals intermingled with these singly-occupied metal-centered orbitals (Figure 12). The HOMO of the anilinopyridinate ligands has a dominant contribution from the *p* orbital on the anilino nitrogen atom, and the combination of four of these orbitals in C_4 symmetry result in *a*, *b*, and *e* combinations. The *b* combination shares symmetry with the Ru_2 δ bonding and antibonding orbitals, and is responsible for the raising of the δ* orbital energy above that of the π* orbitals. However, the *a* and *e* combinations of ap orbitals are also higher in energy than the singly occupied π* orbitals, though spin polarization causes the vacant π* orbitals to be higher in energy. The interloping ligand orbitals have profound implications for higher oxidation state compounds, as oxidation beyond Ru_2^{6+} would likely result in formation of a complex with a ligand radical rather than a formally Ru_2^{7+} core, despite the common practice of labeling the electrochemical feature as $Ru_2^{6+/7+}$. This dicationic compound could have either an $S = 1/2$ or $S = 3/2$ ground electronic state, depending on the nature and magnitude of coupling between the Ru_2 $(\pi^*)^2$ electrons and the ligand radical. While such ligand-based radicals have been invoked for oxidation of Ni_2^{4+} and Pd_2^{4+} paddlewheel-type compounds, further analysis ultimately concluded that oxidation took place from metal-centered orbitals, resulting in Ni_2^{5+} and Pd_2^{5+} species.[71-73] Based on the robust computational methods and strong agreement with experimental measures, we are confident in the orbital assignments depicted here. One further prediction that can be made on the basis of this electronic structure is that true Ru_2^{7+} species will only be accessible if they are supported by π-donor axial ligands strongly donating enough to raise the π* orbitals above the ligand orbitals, as would be expected for the oxo or nitrido complexes postulated as important intermediates in previous studies.[30-32, 36-39]

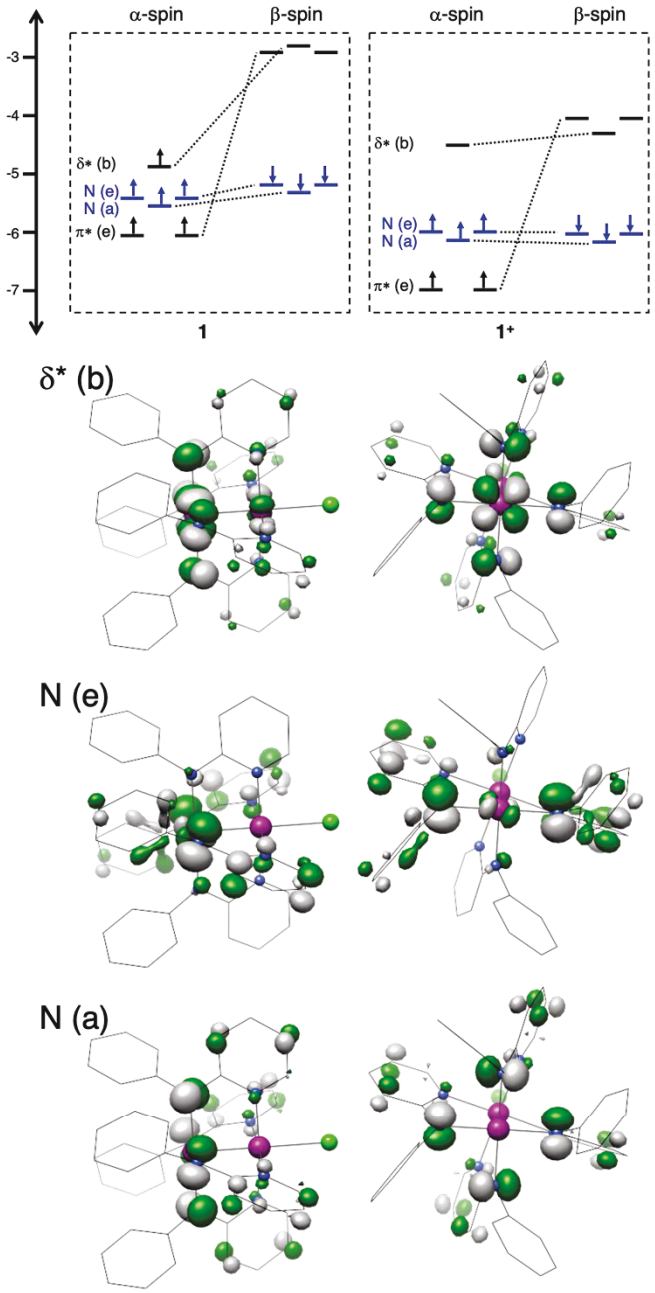

*Figure 12. Calculated orbital energy level diagram for **1** (top left) and **1**$^{+}$ (top right) with ligand-based orbitals highlighted in blue. Boundary surface plots of the δ*, N (e), and N(a) α-spin orbitals for **1**$^{+}$ from top to bottom, viewed along two different axes (left, right). Full 3D models of these orbitals are available in the Supporting Information.*

Conclusions

We present here synthesis and characterization for several novel Ru_2 paddlewheel complexes in both the Ru_2^{5+} and Ru_2^{6+} oxidation states, with ^{1}H NMR analysis offering a previously untapped wealth of information. Trends in reduction potential based on ligand substitution extend previous work for new electron-rich ligands. Comprehensive analysis of the Ru_2^{6+} oxidation state confirms the expected $(\pi^*)^2$ ground electronic state, and the DFT calculated electronic structure indicates that the actual highest occupied molecular orbitals are ligand-based,

explaining why attempts to isolate more oxidized diruthenium compounds have been largely unsuccessful in the past.

Experimental

Physical Measurements

Electrospray ionization mass spectrometry was performed with a Thermo Q Exactive Plus mass spectrometer. IR spectra were recorded with a Bruker Tensor 27 spectrometer using an ATR adapter. Vis/NIR spectra were obtained using a StellarNet tungsten halogen source, a BLACK-Comet UV/Vis spectrometer, and a DWARF-Star NIR spectrometer equipped with a 10 mm path length dip probe tip. Elemental analysis was performed by Midwest Microlab, LLC in Indianapolis, IN, USA. ^{1}H NMR spectra were recorded on 400 MHz and 500 MHz Bruker Avance III spectrometers.

Crystallography

Crystallographc data were collected at the Molecular Structure Laboratory of the Chemistry Department of the University of Wisconsin-Madison. Suitable single crystals of **2**-**4**, **2'**, and [**1**-**4**][$SbCl_6$] were selected under oil and ambient conditions. The crystals were attached to the tip of a MiTeGen MicroMount©, mounted in a stream of cold nitrogen at 100(1) K, and centered in the X-ray beam using a video monitoring system. Crystal evaluation and data collection were performed on a Bruker Quazar SMART APEX-II diffractometer with Mo Kα (λ = 0.71073 Å) radiation. The data were collected using a routine to survey reciprocal space and were indexed by the APEX program.[74] The structures were solved *via* intrinsic phasing and refined by iterative cycles of least-squares refinement on F^2 followed by difference Fourier synthesis. All hydrogen atoms were included in the final structure factor calculation at idealized positions and were allowed to ride on the neighboring atoms with relative isotropic displacement coefficients. Absorption corrections were based on a fitted function to the empirical transmission surface as sampled by multiple equivalent measurements.[75] A highly disordered CH_2Cl_2 molecule was present in the structure of [**4**][$SbCl_6$]. The dataset was treated with SQUEEZE and approximately 43 electrons (c.f., CH_2Cl_2 contains 42 electrons) were accounted for in the solvent accessible void.[76] Crystallographic solution and refinement parameters are given in Table 2.

Electrochemistry

Electrochemical experiments were performed in a nitrogen-filled glovebox using a BioLogic SP-200 potentiostat in dry, degassed CH_2Cl_2 (Fisher, HPLC-grade, non-stabilized) containing 100 mM Bu_4NPF_6 (tetrabutylammonium hexafluorophosphate, Aldrich, 98%) as the supporting electrolyte. Bu_4NPF_6 was purified by thermal recrystallization from ethyl acetate prior to use. A three-electrode setup was employed in all cyclic voltammetry and differential pulse voltammetry experiments, using a glassy carbon disk working electrode (3 mm diameter, CH Instruments), a platinum wire counter electrode (CH Instruments), and a silver wire reference electrode and capillary (Pine Research). The glassy carbon working electrode was polished with an alumina and water slurry (0.05 µm particle size, BASi Research Products), rinsed with methanol, and dried before use. All working electrode potentials were measured versus a $Ag/AgNO_3$ reference electrode containing an internal solution of 100 mM Bu_4NPF_6 and 10 mM $AgNO_3$ in CH_3CN. The Ag electrode was lightly polished with 600 grit sandpaper to remove any surface corrosion

before use. Solid ferrocene was dissolved in analyte solution at the end of each experiment to provide an internal reference for calibrating potentials to the $Fc^{0/+}$ redox couple in CH_2Cl_2.

X-ray Absorption Spectroscopy

Solid samples were diluted in BN, finely ground in an agate mortar, pressed into 1 mm Al spacers, and sealed with 38 μm Kapton tape. Ru K-edge XAS spectra were collected at the Stanford Synchrotron Radiation Lightsource (SSRL) at beamline 9-3. Beamline 9-3 is equipped with a 16-pole, 2-Tesla wiggler source. Incident X-ray radiation was monochromated using a double Si(220) crystal monochromator; samples were maintained at 10 K in a liquid He cryostat during data collection. Spectra were collected in fluorescence mode, with X-rays detected by a passivated implanted planar silicon (PIPS) detector placed at a 90° angle to the sample. Inelastic scatter was attenuated using Soller slits fitted with a Mo filter. Ru foil and a third ionization chamber upstream of the sample were used for internal energy calibration, setting the first inflection point of the Ru foil scan to 22117.0 eV. Data were collected from 21890 to 23111 eV ($k = 16$ Å^{-1}). Two to four scans were averaged and processed using the program Athena of the Demeter package.[77] A smooth pre-edge background was removed from each averaged spectrum by fitting a second-order polynomial to the pre-edge region and subtracting this polynomial from the entire spectrum. A polynomial spline was subtracted above $E_0 = 22130$ eV and the data were normalized in the post-edge absorption to 1.0. Extended X-ray absorption fine structure (EXAFS) fitting was performed using FEFF6 calculations as implemented in the program Artemis, also part of the Demeter package. Scattering paths were initially determined from FEFF calculations using input coordinates based on the X-ray crystal structure of **1**. Paths were optimized by least-squares fitting, where floated parameters included the interatomic scattering distances (R), and the Debye-Waller thermal factors (σ^2).

Magnetometry

SQUID data were collected on a powder sample of **1**[$SbCl_6$] contained in a gel capsule using a Quantum Design MPMS 3 SQUID magnetometer. Magnetic susceptibility data were collected in an externally applied magnetic field of 0.1 T (1000 G) from 2 to 300 K. Magnetization data were collected at 2, 4, 8, and 12 K from 0–7 T, but saturation behavior was not observed at any temperature and these data were not fitted. Magnetic susceptibility data were fitted using the software program PHI.[78] A range of different fitting models were examined, including ones in which the *g* tensor was refined isotropically or anisotropically, and with either both axial and rhombic ZFS tensor components or just an axial component. Ultimately, we selected a model that provided the best fit to the data with the smallest number of unique parameters that gave well-defined and physically reasonable results. In the final model, the *g* value was fixed at 2.00 and the rhombic ZFS component (*E*) was omitted as it had no impact on the fit.

Magnetic Circular Dichroism (MCD)

A mull of **1**[$SbCl_6$] was prepared by grinding a powder sample with poly(dimthylsiloxane). The mull was pressed between quartz windows and mounted in an MCD cell before being flash frozen with liquid nitrogen. MCD spectra were collected at 4.5 K and 3, 5, and 7 T using a Jasco J-1700 spectropolarimeter and an Oxford SM4000-8T Spectromag controlled by a Mercuty iTC temperature controller and a Mercury iPS power supply.

Resonance Raman Spectroscopy

Resonance Raman data were collected on a frozen solution sample of **1**[PF_6] dissolved in CH_2Cl_2 mounted in a quartz finger dewar filled with liquid nitrogen. A Coherent I-305 Ar^+ ion laser (514.5 nm) was used as the excitation source, and ~135° backscattered light was dispersed by an Acton Research triple monochromator equipped with 1200 and 2400 grooves/mm gratings. Dispersed light was analyzed by a Princeton Instruments Spec X:100BR deep depletion, back-thinned CCD camera. Data were collected with a laser power of 40 mW at the sample, an integration time of 25 seconds, and averaged over 5 scans.

Computational Methods

Initial coordinates for **1**-**4** and [**1**-**4**]$^+$ were taken from the corresponding crystallographic data. All calculations were carried out with the ORCA (version 4.0.0.2 for geometry and frequency calculations, 4.2.1 for time-dependent DFT) software package.[79] Calculations were performed by unrestricted Kohn-Sham DFT using the B3LYP hybrid functional with the RIJCOSX chain of spheres approximation.[80-83] Ruthenium atoms were modeled with the TZVP basis set. All other atoms were modeled with the def2-SVP basis set.[84] Relativistic effects were treated using the zero-order relativistic approximation (ZORA) Hamiltonian with the SARC/J auxiliary basis set for coulomb fitting.[85, 86] These methods were used to perform geometry optimizations and numerical vibrational frequency analysis on relevant structures. The conductor-like polarizable continuum model (CPCM) was also implemented to model the solvent effects of dichloromethane in all calculations.[87] The Avogadro program[88,89] was used to edit .xyz files, the Jmol program[90] was used to visualize vibrational frequencies, the MultiWFN program[91] was used to visualize molecular orbitals, and final orbital images were generated with the UCSF Chimera package.[92] Calculations were also attempted using the BP86 functional,[93, 94] but calculated reduction potentials did not agree well with experimental measures. Iterative Gaussian multi-peak fitting of the Abs and MCD spectra was conducting using IGOR Pro 8.[95] Abs transitions were modeled as gaussian bands with linewidths of 2000 cm^{-1} and MCD transitions were modeled as gaussian bands with linewidths of 1200 cm^{-1}.

General Methods

Hap was purchased from Accela ChemBio Inc. and sublimed prior to use. Tris(4-bromophenyl)ammoniumyl hexachloroantimonate (magic blue) was purchased from Sigma-Aldrich and used as received. $Ru_2(OAc)_4Cl$ was synthesized following a literature procedure[96] with important modifications.[97] 2-(4-chloroanilino)pyridine, 2-(4-methylanilino)pyridine, 2(-4-methoxyanilino)pyridine, and 2-anilino-5-methylpyridine were prepared by a modified literature procedure.[52] $Ru_2(Xap)_4Cl$ (X = H, Me, OMe) and $Ru_2(a(Me)p)_4Cl$ were prepared according to the literature procedure for $Ru_2(ap)_4Cl$.[47] The hexafluorophosphate analog of magic blue was prepared according to a literature procedure.[54] Inhibitor-free dichloromethane was purchased from Fisher Scientific, distilled from CaH_2 under N_2, stored over molecular sieves, and filtered before use. Inhibitor-free anhydrous diethyl ether was purchased from Sigma-Aldrich, stored over molecular sieves, and filtered before use.

Synthesis of substituted anilinopyridine ligands.[52] 2-Bromopyridine (1 eq) and the substituted aniline (2 eq) were added to an oven-dried Schlenk flask. The flask was evacuated and refilled with nitrogen three times. The reaction mixture was then heated to 140–170 °C and stirred for 3 hours. The crude mixture was cooled and extracted into diethyl ether or dichloromethane and neutralized with saturated aqueous sodium bicarbonate. The organic layer was washed with

additional bicarbonate solution until the aqueous layer remained basic, and the combined aqueous portions were then extracted with additional diethyl ether or dichloromethane. The combined organic fractions were dried with brine and $MgSO_4$. The solvent was removed under vacuum to afford a mixture of product and residual aniline. For H-Clap, H-Meap, and H-a(Me)p, the crude product was recrystallized from boiling hexanes. For H-OMeap, the crude product was purified by column chromatography (1:1 ethyl acetate and hexanes on silica). All ligands were then sublimed under dynamic vacuum at 110 °C to afford the colorless product in high purity as determined by ^{1}H NMR.
H-Clap 66% yield. ^{1}H NMR ($CDCl_3$): 8.21 (d 1H), 7.51 (t 1H), 7.31 (m 4H), 6.78 (m 2H), 6.50 (s, b, 1H).
H-Meap 66% yield. ^{1}H NMR ($CDCl_3$): 8.18 (d 1H), 7.46 (t 1H), 7.17 (m 4H), 6.81 (d 1H), 6.70 (t 1H), 6.45 (s, b, 1H), 2.33 (s 3H).
H-OMeap 81% yield. ^{1}H NMR ($CDCl_3$): 8.16 (d 1H), 7.44 (t 1H), 7.24 (d 2H), 6.90 (d 2H), 6.67 (m 2H), 6.31 (s, b, 1H), 3.81 (s 3H).
H-a(Me)p 63% yield. ^{1}H NMR ($CDCl_3$): 8.04 (d 1H), 7.31 (m 5H), 7.01 (t 1H), 6.83 (d 1H), 6.39 (s, b, 1H), 2.23 (s 3H).

General synthesis for $Ru_2(ap)_4Cl$ and analogous complexes. $Ru_2(OAc)_4Cl$ and protio-ligand (~10 mass equivalents; >20 molar equivalents) were added to an oven-dried sublimator. The sublimator was closed without a cold finger, evacuated and refilled with nitrogen three times, then evacuated to a static vacuum. The reaction mixture was then heated to 100-130 °C for 90 minutes. Upon melting of the ligand, the reaction rapidly changed in color from brown to green *via* a blue intermediate. Over the course of the reaction, liberated HOAc condensed on the flask above the reaction mixture. Upon completion of the reaction, the mixture was cooled until it solidified, then the sides of the flask were cleaned to remove HOAc and deposited ligand. A cold finger was fitted to the sublimator, and the system was again evacuated and refilled three times before being evacuated to a dynamic vacuum. The crude mixture was then heated to 100 °C overnight to completely sublime away all excess ligand. The remaining green solid was transferred to a fritted filter and washed with methanol until the filtrate was nearly colorless. The product was then extracted into CH_2Cl_2 and evaporated to dryness to give analytically pure material. Yields: **1** 80-90%; **3** 81-94%; **4** 46-48%; **5** 64%.
Characterization information:
2' could not be isolated from a mixture of **2** and **2'**. However, a characteristic 1:2:1 pattern is observed by ^{1}H NMR, which is most evident with peaks at 42.53, 40.40, and 32.18 ppm, compared to the corresponding peak at 35.96 ppm for **2** (see below). Crystals suitable for X-ray diffraction were grown by slow evaporation from a CH_2Cl_2 solution.
3 MW: 970.52 g mol^{-1}. ESI (*m*/*z*): ([M-Cl]$^+$) 936.18. IR (ATR): 1600, 1539, 1503, 1470, 1433, 1362, 1289, 1256, 1220, 1157, 1109, 1017, 942, 883, 810, 785, 753, 735, 713, 670, 660, 651, 633 cm^{-1}. UV/vis in CH_2Cl_2 λ_{max} (ε) = 433 (5400), 780 nm (6400 mol^{-1} L cm^{-1}). ^{1}H NMR ($CDCl_3$): 36.33 (1H), 6.74 (CH_3), -33.11 (1H), -81.12 (1H). [$C_{48}H_{44}ClN_8Ru_2$]: Calcd C 59.40, H 4.57, N 11.55, found C 59.22, H 4.81, N 11.04. Crystals suitable for X-ray diffraction were grown by slow evaporation from a CH_2Cl_2 solution.
4 MW: 1034.52 g mol^{-1}. ESI (*m*/*z*): ([M-Cl]$^+$) 1000.16. IR (ATR): 1591, 1536, 1502, 1465, 1434, 1355, 1292, 1261, 1239, 1218, 1175, 1165, 1151, 1103, 1027, 961, 878, 841, 822, 782, 756, 733, 722, 652 cm^{-1}. UV/Vis in CH_2Cl_2 λ_{max} (ε) = 425 (5800), 788 nm (5900 mol^{-1} L cm^{-1}). **4** was not sufficiently soluble for acquisition of ^{1}H NMR data. [$C_{48}H_{44}ClN_8O_4Ru_2$] Calcd C 55.73, H 4.29,

N 10.83, found C 55.86, H 4.31, N 10.70. Crystals suitable for X-ray diffraction were grown by slow evaporation from a trifluoroethanol solution.
5 MW: 970.52 g mol^{-1}. ESI ([M-Cl]$^+$) 936.18. IR (ATR): 1617, 1590, 1538, 1483, 1447, 1395, 1379, 1350, 1291, 1231, 1207, 1143, 1072, 1041, 920, 866, 814, 750, 730, 696, 677 cm^{-1}. ^{1}H NMR ($CDCl_3$): 37.33 (1H), 4.71 (CH_3), -2.29 (1H), -33.98 (1H). [$C_{48}H_{44}ClN_8Ru_2$]: Calcd C 59.40, H 4.57, N 11.55, found C 58.81, H 4.75, N 11.75.

Synthesis of (4,0) Ru_2(Clap)$_4$Cl (**2**). Attempted synthesis of **2** by the same method as other Ru_2(Xap)$_4$Cl compounds resulted in a (3,1) isomer, where one of the Clap ligands was oriented opposite the other three. To prepare the (4,0) isomer, $Ru_2(OAc)_4Cl$ (300.0 mg, 0.6330 mmol), H-Clap (1.109 g, 5.416 mmol), and LiCl (343.6 mg, 8.106 mmol) were added to an oven-dried 100 mL Schlenk flask. The flask was evacuated and refilled with N_2 three times, and the solids were then dried under active vacuum at 80 °C for one hour. The Schlenk flask was fitted with a reflux condenser and Soxhlet extractor with a cellulose thimble containing K_2CO_3. 50 mL anhydrous toluene was added, and the mixture was brought to reflux at 140 °C for 3 days. The solvent was then removed under vacuum and the solid residue was extracted through a medium fritted filter with CH_2Cl_2 (> 3 L). The CH_2Cl_2 was removed under vacuum and the solid was placed in a sublimator. Excess ligand was removed by sublimation under active vacuum at 110 °C overnight. The remaining solid was redissolved in CH_2Cl_2, filtered through a medium fritted filter, and dried under vacuum. Yield: 235.5 mg, 35% (up to 44% in other trials). MW: 1052.19 g mol^{-1}. ESI (*m*/*z*): ([M-Cl]$^+$) 1017.96. IR (ATR): 1600, 1483, 1468, 1434, 1361, 1289, 1283, 1217, 1159, 1090, 1018, 900, 884, 802, 757, 736, 725, 697 cm^{-1}. UV/vis in CH_2Cl_2 λ_{max} (ε) = 421 (5900), 785 nm (6300 mol^{-1} L cm^{-1}). ^{1}H NMR ($CDCl_3$): 35.96 (1H), -32.84 (1H), -76.84 (1H). [$C_{44}H_{32}Cl_5N_8Ru_2$•$2CH_2Cl_2$] Calcd C 45.21, H 2.97, N 9.17, found C 45.01, H 2.86, N 9.17. Crystals suitable for X-ray diffraction were grown by slow evaporation from a CH_2Cl_2 solution.

Oxidation of Ru_2(Xap)$_4$Cl with MB-$SbCl_6$ or MB-PF_6 [MB = Magic Blue, tris(4-bromophenyl)ammoniumyl cation]. In a glovebox with a dry N_2 atmosphere, Ru_2(Xap)$_4$Cl and one equivalent of the desired MB salt were added to a Schlenk flask and dissolved in CH_2Cl_2 at roughly 6 mg Ru_2(Xap)$_4$Cl / 1 mL CH_2Cl_2 concentration. An immediate color change to red/purple was noticed. The solution was stirred for 30-60 minutes before 3 volume equivalents of diethyl ether was added. The solid product was then collected by filtration in air. Yield: 71-86%.
Characterization information:
[**1**][$SbCl_6$] MW: 1248.88 g mol^{-1}; [**1**][PF_6] MW: 1059.37 g mol^{-1}. ESI (*m*/*z*): ([M_{cat}]$^+$) 915.09. IR (ATR): 1597, 1478, 1462, 1429, 1336, 1292, 1257, 1208, 1162, 1115, 1073, 1053, 1018, 1001, 923, 871, 766, 734, 696, 676, 649 cm^{-1}; 833 cm^{-1} (PF_6^-) for [**1**][PF_6], but the expected peak for $SbCl_6^-$ is too low in energy to be detected (expected ~ 353[98]). UV/vis in CH_2Cl_2 λ_{max} (ε) = 439 (5500), 516 (5900), 981 nm (13000 mol^{-1} L cm^{-1}). ^{1}H NMR (**1**[$SbCl_6$] in $CDCl_3$): 27.06 (d 1H), 13.50 (d 1H), 6.91 (t 1H), 5.98 (t 1H), 3.76 (b 2H), -13.45 (1H); (**1**[PF_6] in CD_2Cl_2): 27.15 (d 1H), 13.35 (d 1H), 6.93 (t 1H), 5.99 (t 1H), 3.76 (b 2H), -13.43 (1H).
[$C_{44}H_{36}Cl_7N_8Ru_2Sb$•$CH_2Cl_2$]: Calcd C 40.52, H 2.87, N 8.40, found C 40.38, H 2.85, N 8.35. Crystals suitable for X-ray diffraction were grown by vapor diffusion of diethyl ether to a saturated CH_2Cl_2 solution.
[**2**][$SbCl_6$] MW: 1386.66 g mol^{-1}; [**1**][PF_6] MW: 1197.15 g mol^{-1}. ESI (*m*/*z*): ([M_{cat}-Cl]$^+$) 1017.96. IR (ATR): 1597, 1482, 1463, 1432, 1400, 1340, 1292, 1253, 1208, 1162, 1093, 1011,

942, 899, 887, 812, 765, 734, 699, 649 cm^{-1}; 839 cm^{-1} (PF_6^-) for [**1**][PF_6]. UV/vis in CH_2Cl_2 λ_{max} (ε) = 450 (5200), 520 (5000), 994 nm (11000 mol^{-1} L cm^{-1}). ^1H NMR (**2**[$SbCl_6$] in CD_2Cl_2): 25.91 (1H), 13.80 (d 1H), 7.12 (t 1H), 4.26 (b 2H), -13.24 (1H). [$C_{44}H_{32}Cl_{11}N_8Ru_2Sb$] Calcd C 38.11, H 2.33, N 8.08, found C 37.93, H 2.38, N 7.87. Crystals suitable for X-ray diffraction were grown by vapor diffusion of diethyl ether to a saturated CH_2Cl_2 solution.
[**3**][$SbCl_6$] MW: 1304.99 g mol^{-1}; [**1**][PF_6] MW: 1179.47 g mol^{-1}. ESI (*m*/*z*): ([M_{cat}]$^+$) 971.15. IR (ATR): 1597, 1500, 1461, 1424, 1343, 1290, 1254, 1211, 1177, 1160, 1113, 1050, 1016, 942, 885, 808, 785, 772, 738, 712, 666, 647, 638 cm^{-1}; 835 cm^{-1} (PF_6^-) for [**1**][PF_6]. UV/vis in CH_2Cl_2 λ_{max} (ε) = 452 (5400), 529 (5500), 989 nm (12000 mol^{-1} L cm^{-1}). ^1H NMR (**3**[$SbCl_6$] in $CDCl_3$): 27.26 (1H), 12.54 (1H), 6.80 (t 1H), 3.63 (b 2H), 0.98 (CH_3), -13.03 (1H); (**3**[PF_6] in CD_2Cl_2): 27.04 (1H), 12.56 (1H), 6.83 (t 1H), 3.64 (b 2H), 0.95 (CH_3), -13.01 (1H). [$C_{48}H_{44}Cl_7N_8Ru_2Sb$] Calcd C 44.18, H 3.40, N 8.59, found C 44.20, H 3.62, N 8.06. Crystals suitable for X-ray diffraction were grown by vapor diffusion of diethyl ether to a saturated CH_2Cl_2 solution.
[**4**][$SbCl_6$] MW: 1368.98 g mol^{-1}; [**1**][PF_6] MW: 1115.47 g mol^{-1}. ESI (*m*/*z*): ([M_{cat}]$^+$) 1035.13. IR (ATR): 1597, 1575, 1500, 1460, 1427, 1335, 1302, 1292, 1248, 1212, 1185, 1167, 1107, 1035, 937, 882, 824, 809, 786, 772, 759, 736, 717, 661, 649, 633 cm^{-1}; 840 cm^{-1} (PF_6^-) for [**1**][PF_6]. UV/vis in CH_2Cl_2 λ_{max} (ε) = 450 (6000), 549 (7400), 1018 nm (13000 mol^{-1} L cm^{-1}). ^1H NMR (**4**[$SbCl_6$] in $CDCl_3$): 26.16 (1H), 10.55 (1H), 6.46 (1H), 4.10 (b 2H), -2.59 (OCH_3), -12.60 (1H). [$C_{48}H_{44}Cl_7N_8O_4Ru_2Sb$] Calcd C 42.11, H 3.24, N 8.19, found C 41.74, H 3.30, N 7.91. Crystals suitable for X-ray diffraction were grown by vapor diffusion of diethyl ether to a saturated CH_2Cl_2 solution.
[**5**][$SbCl_6$] MW: 1304.99 g mol^{-1}. ESI (*m*/*z*): ([M_{cat}]$^+$) 971.15. IR (ATR): 1472, 1376, 1328, 1257, 1203, 924, 876, 814, 756, 736, 695, 667, 644 cm^{-1}. ^1H NMR (**5**[$SbCl_6$] in $CDCl_3$): 24.38 (1H), 8.09 (d 1H), 5.48 (1H) 4.22 (b 2H), -2.73 (CH_3), -14.34 (1H).
[$C_{48}H_{44}Cl_7N_8Ru_2Sb$•$2CH_2Cl_2$] Calcd C 40.72, H 3.28, N 7.60, found C 40.50, H 3.36, N 7.61.

Associated Content

The Supporting Information contains information on the diamagnetic correction for magnetic susceptibility measurements, additional figures for NMR (Figures S1-S5), electrochemistry (Figures S6-S10), EXAFS (Figures 11-13), electronic absorption spectra (Figures S14-16), reduced magnetization (Figure S17), and calculated linear free energy relationships (Figure S18), as well as optimized XYZ coordinates for all calculated structures.

CCDC codes 1871323 and 2098290-2098296 contain the supplementary crystallographic data for this paper.

Author Information

Corresponding Author

John F. Berry – *Department of Chemistry, University of Wisconsin-Madison, Madison, Wisconsin 53706, United States*; orcid.org/0000-0002-6805-0640; Email: berry@chem.wisc.edu.

Authors

Michael D. Roy – *Department of Chemistry, University of Wisconsin-Madison, Madison, Wisconsin 53706, United States.*

Michael J. Trenerry – *Department of Chemistry, University of Wisconsin-Madison, Madison, Wisconsin 53706, United States.*

Biswash Thakuri – *Department of Chemistry, University of Vermont, Burlington, Vermont 05405, United States.*

Samantha N. MacMillan – *Department of Chemistry and Chemical Biology, Cornell University, Ithaca, New York 14853, United States;* orcid.org/0000-0001-6516-1823.

Matthew D. Liptak – *Department of Chemistry, University of Vermont, Burlington, Vermont 05405, United States;* orcid.org/0000-0002-4951-6636.

Kyle M. Lancaster – *Department of Chemistry and Chemical Biology, Cornell University, Ithaca, New York 14853, United States;* orcid.org/0000-0001-7296-128X.

Acknowledgements

MDR would like to thank Rebeca L. Fernandez for assistance with resonance Raman spectroscopy, Thomas C. Brunold for insights on MCD spectroscopy and electronic structure calculations, and Michael M. Aristov for crystallography assistance and 3D animations. MDL would like to thank Dzmitry Parul (Jasco) and Doug Gomez (UVM) for their assistance in implementing a single instrument UV/Vis/nIR MCD setup.

We thank the U.S. Department of Energy, Chemical Sciences, Geosciences, and Biosciences Division, Office of Basic Energy Sciences, Office of Science (DE-SC0021021) for funding this research. NMR spectrometers were supported by NSF grant CHE-1048642 and a generous gift from Paul J. and Margaret M. Bender. The mass spectrometer was supported by NIH grant 1S10 OD020022-1. The X-ray diffractometer was supported by a generous gift from Paul J. and Margaret M. Bender. The Quantum Design MPMS3 magnetometer was supported by the UW-Madison Department of Chemistry. Molecular orbital graphics were generated with UCSF Chimera, developed by the Resource for Biocomputing, Visualization, and Informatics at the University of California, San Francisco, with support from NIH grant P41-GM103311.

KML acknowledges NSF (CHE-1954515) for support. XAS data were obtained at the Stanford Synchrotron Radiation Lightsource, SLAC National Accelerator Laboratory, which is supported by the US Department of Energy, Office of Science, Office of Basic Energy Sciences, under Contract No. DE-AC02-76SF00515. The SSRL Structural Molecular Biology Program is supported by the DOE Office of Biological and Environmental Research, and by the National Institutes of Health, National Institute of General Medical Sciences (P30GM133894).

References

1. Chiarella, G. M.; Cotton, F. A.; Murillo, C. A.; Ventura, K.; Villagrán, D.; Wang, X., Manipulating Magnetism: Ru_2^{5+} Paddlewheels Devoid of Axial Interactions. *J. Am. Chem. Soc.* **2014,** *136* (27), 9580-9589.

2. Mikuriya, M.; Yoshioka, D.; Handa, M., Magnetic interactions in one-, two-, and three-dimensional assemblies of dinuclear ruthenium carboxylates. *Coord. Chem. Rev.* **2006,** *250* (17), 2194-2211.

3. Miyasaka, H.; Clérac, R.; Campos-Fernández, C. S.; Dunbar, K. R., The first crystal structure of a one-dimensional chain of linked Ru^{II}=Ru^{II} units. *J. Chem. Soc. Dalton Trans.* **2001,** (6), 858-861.

4. O'Neal, K. R.; Liu, Z.; Miller, J. S.; Fishman, R. S.; Musfeldt, J. L., Pressure-driven high-to-low spin transition in the bimetallic quantum magnet $[Ru_2(O_2CMe)_4][Cr(CN)_6]$. *Phys. Rev. B* **2014,** *90* (10), 104301.

5. Su, S.-D.; Zhu, X.-Q.; Wen, Y.-H.; Zhang, L.-T.; Yang, Y.-Y.; Lin, C.-S.; Wu, X.-T.; Sheng, T.-L., A Diruthenium-Based Mixed Spin Complex Ru_2^{5+}(*S*=1/2)-CN-Ru_2^{5+}(*S*=3/2). *Angew. Chem. Int. Ed.* **2019,** *58* (43), 15344-15348.
6. Uemura, K.; Uesugi, N.; Matsuyama, A.; Ebihara, M.; Yoshikawa, H.; Awaga, K., Integration of Paramagnetic Diruthenium Complexes into an Extended Chain by Heterometallic Metal–Metal Bonds with Diplatinum Complexes. *Inorg. Chem.* **2016,** *55* (14), 7003-7011.
7. Yang, B.-B.; Feng, L.-N.; Fan, X.-M.; Zhang, K.-X.; Yang, J.-H.; Liu, B., Towards a new type of heterometallic system based on a paddle-wheel Ru_2 dimer: first results derived from the use of a high spin diruthenium(III,III) building block. *Inorg. Chem. Front.* **2017,** *4* (6), 1061-1065.
8. Raghavan, A.; Yuan, F.; Ren, T., Drastic Tuning of the Electronic Structures of Diruthenium Aryl Complexes by Isoelectronic Axial Ligands. *Inorg. Chem.* **2020,** *59* (13), 8663-8666.
9. Opperwall, S. R.; Liu, B.; Pilo, A. L.; Cao, Z.; Fanwick, P. E.; Ren, T., Synthesis and characterization of $Ru_2(\eta^2$-D*m*AniF$)_2(\mu$-D*m*AniF$)_2(\mu$-OAc$)(\mu$-O). *Polyhedron* **2016,** *103*, 126-130.
10. Zhang, J.; Kosaka, W.; Sugimoto, K.; Miyasaka, H., Magnetic Sponge Behavior via Electronic State Modulations. *J. Am. Chem. Soc.* **2018,** *140* (16), 5644-5652.
11. Miyasaka, H., Control of Charge Transfer in Donor/Acceptor Metal–Organic Frameworks. *Acc. Chem. Res.* **2013,** *46* (2), 248-257.
12. Wang, C.-H.; Gao, W.-Y.; Powers, D. C., Measuring and Modulating Substrate Confinement during Nitrogen-Atom Transfer in a Ru_2-Based Metal-Organic Framework. *J. Am. Chem. Soc.* **2019,** *141* (49), 19203-19207.
13. Miyasaka, H.; Motokawa, N.; Matsunaga, S.; Yamashita, M.; Sugimoto, K.; Mori, T.; Toyota, N.; Dunbar, K. R., Control of Charge Transfer in a Series of $Ru_2^{II,II}$/TCNQ Two-Dimensional Networks by Tuning the Electron Affinity of TCNQ Units: A Route to Synergistic Magnetic/Conducting Materials. *J. Am. Chem. Soc.* **2010,** *132* (5), 1532-1544.
14. Alves Rico, S. R.; Abbasi, A. Z.; Ribeiro, G.; Ahmed, T.; Wu, X. Y.; de Oliveira Silva, D., Diruthenium(II,III) metallodrugs of ibuprofen and naproxen encapsulated in intravenously injectable polymer–lipid nanoparticles exhibit enhanced activity against breast and prostate cancer cells. *Nanoscale* **2017,** *9* (30), 10701-10714.
15. Benadiba, M.; de M. Costa, I.; Santos, R. L. S. R.; Serachi, F. O.; de Oliveira Silva, D.; Colquhoun, A., Growth inhibitory effects of the Diruthenium-Ibuprofen compound, $[Ru_2Cl(Ibp)_4]$, in human glioma cells in vitro and in the rat C6 orthotopic glioma in vivo. *J. Biol. Inorg. Chem.* **2014,** *19* (6), 1025-1035.
16. Hanif Ur, R.; Freitas, T. E.; Gomes, R. N.; Colquhoun, A.; de Oliveira Silva, D., Axially-modified paddlewheel diruthenium(II,III)-ibuprofenato metallodrugs and the influence of the structural modification on U87MG and A172 human glioma cell proliferation, apoptosis, mitosis and migration. *J. Inorg. Biochem.* **2016,** *165*, 181-191.
17. Johnpeter, J. P.; Schmitt, F.; Denoyelle-Di-Muro, E.; Wagnières, G.; Juillerat-Jeanneret, L.; Therrien, B., Photoactive sawhorse-type diruthenium tetracarbonyl complexes. *Inorg. Chim. Acta* **2012,** *393*, 246-251.
18. Koceva-Chyła, A.; Matczak, K.; Hikisz, M. P.; Durka, M. K.; Kochel, M. K.; Süss-Fink, G.; Furrer, J.; Kowalski, K., Insights into the in vitro Anticancer Effects of Diruthenium-1. *ChemMedChem* **2016,** *11* (19), 2171-2187.

19. Osterloh, W. R.; Galindo, G.; Yates, M. J.; Van Caemelbecke, E.; Kadish, K. M., Synthesis, Structural and Physicochemical Properties of Water-Soluble Mixed-Ligand Diruthenium Complexes Containing Anilinopyridinate Bridging Ligands. *Inorg. Chem.* **2020,** *59* (1), 584-594.
20. Ribeiro, G.; Benadiba, M.; de Oliveira Silva, D.; Colquhoun, A., The novel ruthenium—γ-linolenic complex [Ru_2(aGLA)$_4$Cl] inhibits C6 rat glioma cell proliferation and induces changes in mitochondrial membrane potential, increased reactive oxygen species generation and apoptosis in vitro. *Cell Biochem. Funct.* **2010,** *28* (1), 15-23.
21. Delgado-Martínez, P.; González-Prieto, R.; Gómez-García, C. J.; Jiménez-Aparicio, R.; Priego, J. L.; Torres, M. R., Structural, magnetic and electrical properties of one-dimensional tetraamidatodiruthenium compounds. *Dalton Trans.* **2014,** *43* (8), 3227-3237.
22. Jiang, K.; Pookpanratana, S. J.; Ren, T.; Natoli, S. N.; Sperling, B. A.; Robertson, J.; Richter, C. A.; Yu, S.; Li, Q., Nonvolatile memory based on redox-active ruthenium molecular monolayers. *Appl. Phys. Lett.* **2019,** *115* (16), 162102.
23. Pookpanratana, S.; Zhu, H.; Bittle, E. G.; Natoli, S. N.; Ren, T.; Richter, C. A.; Li, Q.; Hacker, C. A., Non-volatile memory devices with redox-active diruthenium molecular compound. *J. Phys. Condens. Matter* **2016,** *28* (9), 094009.
24. Ren, T.; Zou, G.; Alvarez, J. C., Facile electronic communication between bimetallic termini bridged by elemental carbon chains. *Chem. Commun.* **2000,** (13), 1197-1198.
25. Ren, T., Diruthenium *σ*-Alkynyl Compounds: A New Class of Conjugated Organometallics. *Organometallics* **2005,** *24* (21), 4854-4870.
26. Ying, J.-W.; Cao, Z.; Campana, C.; Song, Y.; Zuo, J.-L.; Tyler, S. F.; Ren, T., Linear trimers of diruthenium linked by polyyndiyl or phenylenediethynyl bridges: A family of unique electronic wires. *Polyhedron* **2015,** *86*, 76-80.
27. Cao, Z.; Xi, B.; Jodoin, D. S.; Zhang, L.; Cummings, S. P.; Gao, Y.; Tyler, S. F.; Fanwick, P. E.; Crutchley, R. J.; Ren, T., Diruthenium–Polyyn-diyl–Diruthenium Wires: Electronic Coupling in the Long Distance Regime. *J. Am. Chem. Soc.* **2014,** *136* (34), 12174-12183.
28. Das, A.; Reibenspies, J. H.; Chen, Y.-S.; Powers, D. C., Direct Characterization of a Reactive Lattice-Confined Ru_2 Nitride by Photocrystallography. *J. Am. Chem. Soc.* **2017,** *139* (8), 2912-2915.
29. Harvey, M. E.; Musaev, D. G.; Du Bois, J., A Diruthenium Catalyst for Selective, Intramolecular Allylic C–H Amination: Reaction Development and Mechanistic Insight Gained through Experiment and Theory. *J. Am. Chem. Soc.* **2011,** *133* (43), 17207-17216.
30. Musch Long, A. K.; Yu, R. P.; Timmer, G. H.; Berry, J. F., Aryl C−H Bond Amination by an Electrophilic Diruthenium Nitride. *J. Am. Chem. Soc.* **2010,** *132* (35), 12228-12230.
31. Musch Long, A. K.; Timmer, G. H.; Pap, J. S.; Snyder, J. L.; Yu, R. P.; Berry, J. F., Aryl C–H Amination by Diruthenium Nitrides in the Solid State and in Solution at Room Temperature: Experimental and Computational Study of the Reaction Mechanism. *J. Am. Chem. Soc.* **2011,** *133* (33), 13138-13150.
32. Corcos, A. R.; Long, A. K. M.; Guzei, I. A.; Berry, J. F., A Synthetic Cycle for Nitrogen Atom Transfer Featuring a Diruthenium Nitride Intermediate. *Eur. J. Inorg. Chem.* **2013,** *2013* (22-23), 3808-3811.
33. Corcos, A. R.; Berry, J. F., Anilinopyridinate-supported Ru_2^{x+} (x = 5 or 6) paddlewheel complexes with labile axial ligands. *Dalton Trans.* **2017,** *46* (17), 5532-5539.

34. Angaridis, P., Ruthenium Compounds. In *Multiple Bonds Between Metal Atoms*, Cotton, F. A.; Murillo, C. A.; Walton, R. A., Eds. Springer: Boston, MA, 2005.
35. Corcos, A. R.; Roy, M. D.; Killian, M. M.; Dillon, S.; Brunold, T. C.; Berry, J. F., Electronic Structure of Anilinopyridinate-Supported Ru_2^{5+} Paddlewheel Compounds. *Inorg. Chem.* **2017,** *56* (23), 14662-14670.
36. Corcos, A. R.; Pap, J. S.; Yang, T.; Berry, J. F., A Synthetic Oxygen Atom Transfer Photocycle from a Diruthenium Oxyanion Complex. *J. Am. Chem. Soc.* **2016,** *138* (31), 10032-10040.
37. Villalobos, L.; Barker Paredes, J. E.; Cao, Z.; Ren, T., *tert*-Butyl Hydroperoxide Oxygenation of Organic Sulfides Catalyzed by Diruthenium(II,III) Tetracarboxylates. *Inorg. Chem.* **2013,** *52* (21), 12545-12552.
38. Thompson, D. J.; Barker Paredes, J. E.; Villalobos, L.; Ciclosi, M.; Elsby, R. J.; Liu, B.; Fanwick, P. E.; Ren, T., Diruthenium(II,III) tetracarboxylates catalyzed H_2O_2 oxygenation of organic sulfides. *Inorg. Chim. Acta* **2015,** *424*, 150-155.
39. Goberna-Ferrón, S.; Peña, B.; Soriano-López, J.; Carbó, J. J.; Zhao, H.; Poblet, J. M.; Dunbar, K. R.; Galán-Mascarós, J. R., A fast metal–metal bonded water oxidation catalyst. *J. Catal.* **2014,** *315*, 25-32.
40. Raghavan, A.; Ren, T., Bisaryl Diruthenium(III) Paddlewheel Complexes: Synthesis and Characterization. *Organometallics* **2019,** *38* (19), 3888-3896.
41. Natoli, S. N.; Zeller, M.; Ren, T., Diruthenium-DMBA compounds bearing extended cross-conjugated ligands. *J. Organomet. Chem.* **2017,** *847*, 90-96.
42. Savchenko, J.; Cao, Z.; Natoli, S. N.; Cummings, S. P.; Prentice, B. M.; Fanwick, P. E.; Ren, T., New Diruthenium Bis-alkynyl Compounds as Potential Ditopic Linkers. *Organometallics* **2013,** *32* (21), 6461-6467.
43. Bear, J. L.; Li, Y.; Han, B.; Kadish, K. M., Synthesis, Molecular Structure, and Electrochemistry of a Paramagnetic Diruthenium(III) Complex. Characterization of $Ru_2(hpp)_4Cl_2$, Where hpp Is the 1,3,4,6,7,8- Hexahydro-2H-pyrimido[1,2-a]pyrimidinate Ion. *Inorg. Chem.* **1996,** *35* (5), 1395-1398.
44. Cotton, F. A.; Murillo, C. A.; Reibenspies, J. H.; Villagrán, D.; Wang, X.; Wilkinson, C. C., Paramagnetism at Ambient Temperature, Diamagnetism at Low Temperature in a Ru26+ Core: Structural Evidence for Zero-Field Splitting. *Inorg. Chem.* **2004,** *43* (26), 8373-8378.
45. Xu, G.-L.; Jablonski, C. G.; Ren, T., $Ru_2(DMBA)_4(BF_4)_2$ and $Ru_2(DMBA)_4(NO_3)_2$: the first examples of diruthenium compounds containing BF_4^- and NO_3^- as ligands. *Inorg. Chim. Acta* **2003,** *343*, 387-390.
46. Cotton, F. A.; Yokochi, A., Synthesis, Structure, and Magnetic Properties of New Ru_2^{6+} Compounds. *Inorg. Chem.* **1997,** *36* (4), 567-570.
47. Chakravarty, A. R.; Cotton, F. A.; Tocher, D. A., Syntheses, molecular structures, and properties of two polar diruthenium(II,III) complexes of 2-hydroxypyridine and 2-anilinopyridine. *Inorg. Chem.* **1985,** *24* (2), 172-177.
48. Kadish, K. M.; Wang, L.-L.; Thuriere, A.; Van Caemelbecke, E.; Bear, J. L., Factors Affecting the Electrochemical and Spectroelectrochemical Properties of Diruthenium(III,II) Complexes Containing Four Identical Unsymmetrical Bridging Ligands. *Inorg. Chem.* **2003,** *42* (3), 834-843.
49. Kadish, K. M.; Phan, T. D.; Giribabu, L.; Shao, J.; Wang, L.-L.; Thuriere, A.; Van Caemelbecke, E.; Bear, J. L., Electrochemical and Spectroelectrochemical Characterization of Ru_2^{4+} and Ru_2^{3+} Complexes under a CO Atmosphere. *Inorg. Chem.* **2004,** *43* (3), 1012-1020.

50. Kadish, K. M.; Wang, L.-L.; Thuriere, A.; Giribabu, L.; Garcia, R.; Van Caemelbecke, E.; Bear, J. L., Solvent Effects on the Electrochemistry and Spectroelectrochemistry of Diruthenium Complexes. Studies of $Ru_2(L)_4Cl$ Where L = 2-CH_3ap, 2-Fap, and 2,4,6-F_3ap, and ap is the 2-Anilinopyridinate Anion. *Inorg. Chem.* **2003,** *42* (25), 8309-8319.
51. Van Caemelbecke, E.; Phan, T.; Osterloh, W. R.; Kadish, K. M., Electrochemistry of metal-metal bonded diruthenium complexes. *Coord. Chem. Rev.* **2021,** *434*, 213706.
52. Ito, A.; Fujino, H.; Ushiyama, K.; Yamanaka, E.; Yamasaki, R.; Okamoto, I., Acid-controlled switching of conformational preference of N,N-diarylamides bearing pyridine. *Tetrahedron Lett.* **2016,** *57* (42), 4737-4741.
53. Doyle, M. P.; Bagheri, V.; Wandless, T. J.; Harn, N. K.; Brinker, D. A.; Eagle, C. T.; Loh, K. L., Exceptionally high trans (anti) stereoselectivity in catalytic cyclopropanation reactions. *J. Am. Chem. Soc.* **1990,** *112* (5), 1906-1912.
54. Jahn, U.; Aussieker, S., Triarylaminium Salt Induced Oxidative Cyclizations of Tertiary Amines. Convenient Access to 2-Substituted Pyrrolidinium Salts. *Org. Lett.* **1999,** *1* (6), 849-852.
55. Nguyen, M.; Phan, T.; Caemelbecke, E. V.; Kajonkijya, W.; Bear, J. L.; Kadish, K. M., Interconversion between (3,1) and (4,0) Isomers of $Ru_2(L)_4X$ Complexes where L is 2-Anilinopyridinate or 2-(2,4,6-Trifluoroanilino)pyridinate Anion and X = Cl^- or $C{\equiv}CC_5H_4N^-$. *Inorg. Chem.* **2008,** *47* (17), 7775-7783.
56. Bear and Kadish use the σ_p Hammett parameter to describe the Ru_2(2-Meap)$_4$Cl complex, when the methyl group is actually ortho to the anilino nitrogen of the anilinopyridinate ligand. Compound **3** considered in this work is more appropriately described by the given σ_p Hammett parameter and exhibits redox potentials that more closely fit the overall data trends found for analogously substituted anilinopyridinate complexes.
57. The value of 0.089 V reported by the authors includes 8 compounds, only 4 of which are appropriately parameterized by para- sigma parameters. The value listed here, 0.085 V, was found by linear least squares fitting of the $E_{1/2}$ values for the unsubstituted diphenylformamidinate compounds and the three *para*- substituted ligand compounds, excluding the *meta*- and di- substituted ligand compounds.
58. Lin, C.; Ren, T.; Valente, E. J.; Zubkowski, J. D.; Smith, E. T., Continuous Spectroscopic and Redox Tuning of Dinuclear Compounds: Chlorotetrakis(μ-N,N′-diarylformamidinato)diruthenium(II,III). *Chemistry Letters* **1997,** *26* (8), 753-754.
59. Lin, C.; Protasiewicz, J. D.; Smith, E. T.; Ren, T., Redox tuning of the dimolybdenum compounds at the ligand periphery: a direct correlation with the Hammett constant of the substituents. *J. Chem. Soc. Chem. Commun.* **1995,** (22), 2257-2258.
60. Lin, C.; Protasiewicz, J. D.; Smith, E. T.; Ren, T., Linear Free Energy Relationships in Dinuclear Compounds. 2. Inductive Redox Tuning via Remote Substituents in Quadruply Bonded Dimolybdenum Compounds. *Inorg. Chem.* **1996,** *35* (22), 6422-6428.
61. Connelly, N. G.; Geiger, W. E., Chemical Redox Agents for Organometallic Chemistry. *Chem. Rev.* **1996,** *96* (2), 877-910.
62. Krause, M. O.; Oliver, J. H., Natural widths of atomic *K* and *L* levels, *K*α X-ray lines and several *KLL* Auger lines. *J. Phys. Chem. Ref. Data* **1979,** *8* (2), 329-338.
63. Hämäläinen, K.; Siddons, D. P.; Hastings, J. B.; Berman, L. E., Elimination of the inner-shell lifetime broadening in X-ray-absorption spectroscopy. *Phys. Rev. Lett.* **1991,** *67* (20), 2850-2853.

64. Lima, F. A.; Bjornsson, R.; Weyhermüller, T.; Chandrasekaran, P.; Glatzel, P.; Neese, F.; DeBeer, S., High-resolution molybdenum K-edge X-ray absorption spectroscopy analyzed with time-dependent density functional theory. *Phys. Chem. Chem. Phys.* **2013,** *15* (48), 20911-20920.
65. Pap, J. S.; DeBeer George, S.; Berry, J. F., Delocalized Metal–Metal and Metal–Ligand Multiple Bonding in a Linear Ru–Ru≡N Unit: Elongation of a Traditionally Short Ru≡N Bond. *Angew. Chem. Int. Ed.* **2008,** *47* (52), 10102-10105.
66. Chiarella, G. M.; Cotton, F. A.; Murillo, C. A.; Young, M. D.; Zhao, Q., Large Changes in Electronic Structures of Ru_2^{6+} Species Caused by the Variations of the Bite Angle of Guanidinate Ligands: Tuning Magnetic Behavior. *Inorg. Chem.* **2010,** *49* (6), 3051-3056.
67. Wang, C.-F.; Zuo, J. L.; Ying, J.-W.; Ren, T.; You, X.-Z., Novel Heterometallic Fe−Ru_2−Fe Arrays via "Complex of Complexes" Approach. *Inorg. Chem.* **2008,** *47* (20), 9716-9722.
68. See Phi User Manual. http://www.molmag.manchester.ac.uk/software/phi_manual.pdf
69. Tait, C. D.; Garner, J. M.; Collman, J. P.; Sattelberger, A. P.; Woodruff, W. H., Vibrational study of multiply metal-metal bonded ruthenium porphyrin dimers. *J. Am. Chem. Soc.* **1989,** *111* (20), 7806-7811.
70. Roy, L. E.; Jakubikova, E.; Guthrie, M. G.; Batista, E. R., Calculation of One-Electron Redox Potentials Revisited. Is It Possible to Calculate Accurate Potentials with Density Functional Methods? *J. Phys. Chem. A* **2009,** *113* (24), 6745-6750.
71. Berry, J. F.; Bothe, E.; Cotton, F. A.; Ibragimov, S. A.; Murillo, C. A.; Villagrán, D.; Wang, X., Metal−Metal Bonding in Mixed Valence Ni_2^{5+} Complexes and Spectroscopic Evidence for a Ni_2^{6+} Species. *Inorg. Chem.* **2006,** *45* (11), 4396-4406.
72. Berry, J. F., Two-Center/Three-Electron Sigma Half-Bonds in Main Group and Transition Metal Chemistry. *Acc. Chem. Res.* **2016,** *49* (1), 27-34.
73. Berry, J. F.; Bill, E.; Bothe, E.; Cotton, F. A.; Dalal, N. S.; Ibragimov, S. A.; Kaur, N.; Liu, C. Y.; Murillo, C. A.; Nellutla, S.; North, J. M.; Villagrán, D., A Fractional Bond Order of 1/2 in Pd_2^{5+}−Formamidinate Species; The Value of Very High-Field EPR Spectra. *J. Am. Chem. Soc.* **2007,** *129* (5), 1393-1401.
74. Bruker-AXS (2016). APEX3. Version 2016.5-0. Madison, Wisconsin, USA.
75. Krause, L.; Herbst-Irmer, R.; Sheldrick, G. M.; Stalke, D., Comparison of silver and molybdenum microfocus X-ray sources for single-crystal structure determination. *J. Appl. Crystallogr.* **2015,** *48* (1), 3-10.
76. Spek, A., PLATON SQUEEZE: a tool for the calculation of the disordered solvent contribution to the calculated structure factors. *Acta Crystallogr. C* **2015,** *71* (1), 9-18.
77. Ravel, B.; Newville, M., ATHENA, ARTEMIS, HEPHAESTUS: data analysis for X-ray absorption spectroscopy using IFEFFIT. *J. Synchrotron Rad.* **2005,** *12* (4), 537-541.
78. Chilton, N. F.; Anderson, R. P.; Turner, L. D.; Soncini, A.; Murray, K. S., PHI: A powerful new program for the analysis of anisotropic monomeric and exchange-coupled polynuclear d- and f-block complexes. *J. Comput. Chem.* **2013,** *34* (13), 1164-1175.
79. Neese, F., Software update: the ORCA program system, version 4.0. *WIREs Computational Molecular Science* **2018,** *8* (1), e1327.
80. Neese, F.; Wennmohs, F.; Hansen, A.; Becker, U., Efficient, approximate and parallel Hartree–Fock and hybrid DFT calculations. A 'chain-of-spheres' algorithm for the Hartree–Fock exchange. *Chem. Phys.* **2009,** *356* (1), 98-109.

81. Grimme, S.; Antony, J.; Ehrlich, S.; Krieg, H., A consistent and accurate ab initio parametrization of density functional dispersion correction (DFT-D) for the 94 elements H-Pu. *J. Chem. Phys.* **2010,** *132* (15), 154104.
82. Becke, A. D., Density-functional thermochemistry. III. The role of exact exchange. *J. Chem. Phys.* **1993,** *98* (7), 5648-5652.
83. Lee, C.; Yang, W.; Parr, R. G., Development of the Colle-Salvetti correlation-energy formula into a functional of the electron density. *Phys. Rev. B* **1988,** *37* (2), 785-789.
84. Weigend, F.; Ahlrichs, R., Balanced basis sets of split valence, triple zeta valence and quadruple zeta valence quality for H to Rn: Design and assessment of accuracy. *Phys. Chem. Chem. Phys.* **2005,** *7* (18), 3297-3305.
85. Lenthe, E. v.; Baerends, E. J.; Snijders, J. G., Relativistic regular two-component Hamiltonians. *J. Chem. Phys.* **1993,** *99* (6), 4597-4610.
86. Pantazis, D. A.; Chen, X.-Y.; Landis, C. R.; Neese, F., All-Electron Scalar Relativistic Basis Sets for Third-Row Transition Metal Atoms. *J. Chem. Theory Comput.* **2008,** *4* (6), 908-919.
87. York, D. M.; Karplus, M., A Smooth Solvation Potential Based on the Conductor-Like Screening Model. *J. Phys. Chem. A* **1999,** *103* (50), 11060-11079.
88. Avogadro: an open-source molecular builder and visualization tool. Version 1.XX. http://avogadro.cc/ .
89. Hanwell, M. D.; Curtis, D. E.; Lonie, D. C.; Vandermeersch, T.; Zurek, E.; Hutchison, G. R., Avogadro: an advanced semantic chemical editor, visualization, and analysis platform. *J. Cheminformatics* **2012,** *4* (1), 17.
90. Jmol: an open-source Java viewer for chemical structures in 3D. http://www.jmol.org/ .
91. Lu, T.; Chen, F., Multiwfn: A multifunctional wavefunction analyzer. *J. Comput. Chem.* **2012,** *33* (5), 580-592.
92. Pettersen, E. F.; Goddard, T. D.; Huang, C. C.; Couch, G. S.; Greenblatt, D. M.; Meng, E. C.; Ferrin, T. E., UCSF Chimera—A visualization system for exploratory research and analysis. *J. Comput. Chem.* **2004,** *25* (13), 1605-1612.
93. Perdew, J. P., Density-functional approximation for the correlation energy of the inhomogeneous electron gas. *Phys. Rev. B* **1986,** *33* (12), 8822-8824.
94. Becke, A. D., Density-functional exchange-energy approximation with correct asymptotic behavior. *Phys. Rev. A* **1988,** *38* (6), 3098-3100.
95. Igor Pro 8: a product of WaveMetrics. https://www.wavemetrics.com/software/igor-pro-8
96. Stephenson, T. A.; Wilkinson, G., New ruthenium carboxylate complexes. *J. Inorg. Nuc. Chem.* **1966,** *28* (10), 2285-2291.
97. Brown, T. R.; Dolinar, B. S.; Hillard, E. A.; Clérac, R.; Berry, J. F., Electronic Structure of Ru_2(II,II) Oxypyridinates: Synthetic, Structural, and Theoretical Insights into Axial Ligand Binding. *Inorg. Chem.* **2015,** *54* (17), 8571-8589.
98. Nakamoto, K., Infrared and Raman Spectra of Inorganic and Coordination Compounds. *Handbook of Vibrational Spectroscopy* **2001**.

For Table of Contents Only:

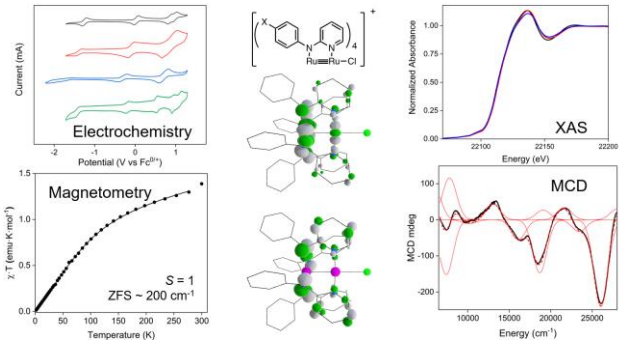

Synopsis: A series of diruthenium paddlewheel complexes in both Ru_2^{5+} and Ru_2^{6+} oxidation states were prepared and their electronic structure was investigated through ^{1}H NMR spectroscopy, electrochemistry, Vis/nIR and MCD spectroscopy, magnetometry, X-ray absorbance spectroscopy, and density functional theory. This study establishes a framework for understanding $S = 1$ Ru_2^{6+} complexes supported by anilinopyridinate ligands.